Multigap topology and non-Abelian braiding of phonons from first principles

Bo Peng [●],[1,*] Adrien Bouhon [●],[2,*] Robert-Jan Slager [●],[1,*] and Bartomeu Monserrat [●][1,3,*]

[1]*TCM Group, Cavendish Laboratory, University of Cambridge, J. J. Thomson Avenue, Cambridge CB3 0HE, United Kingdom*
[2]*Nordic Institute for Theoretical Physics (Nordita), Stockholm University and KTH Royal Institute of Technology,*
Hannes Alfvéns väg 12, Stockholm SE-106 91, Sweden
[3]*Department of Materials Science and Metallurgy, University of Cambridge, 27 Charles Babbage Road,*
Cambridge CB3 0FS, United Kingdom

Non-Abelian states of matter, in which the final state depends on the order of the interchanges of two quasiparticles, can encode information immune from environmental noise with the potential to provide a robust platform for topological quantum computation. We demonstrate that phonons can carry non-Abelian frame charges at the band-crossing points of their frequency spectrum, and that external stimuli can drive their braiding. We present a general framework to understand the topological configurations of phonons from first-principles calculations using a topological invariant called Euler class, and provide a complete analysis of phonon braiding by combining different topological configurations. Taking a well-known dielectric material Al_2O_3 as a representative example, we demonstrate that electrostatic doping gives rise to phonon band inversions that can induce redistribution of the frame charges, leading to non-Abelian braiding of phonons. Our work provides a quasiparticle platform for realizable non-Abelian braiding in *reciprocal space*, and expands the tool set for studying braiding processes.

I. INTRODUCTION

Non-Abelian states of matter arise from noncommutative interchanges of quasiparticles [1]. In this process, called braiding, the winding of one quasiparticle around another can encode information, creating non-Abelian states that are immune from external noise: as long as the braiding occurs, the information is topologically protected. This process can form the basis for topological quantum bits (qubits), and a variety of strategies for non-Abelian braiding have been proposed, including braiding of quasiparticles in intrinsic topological states such as fractional quantum Hall systems [2], and also in symmetry-protected topological states such as half-quantum vortices in superconductors with *p*-wave symmetry [3] and Majorana modes in hybrid systems [4]. Multiple variants of these proposed architectures exist [5,6], and experimental evidence has started to emerge in the past few years [7,8], providing a proof of principle for the existence of non-Abelian quasiparticles. However, multiple difficulties remain in exploiting these quasiparticles for braiding, for example, Majorana fermions are boundary states that have proven challenging to observe [9]. It would therefore be desirable to find alternative platforms in which non-Abelian braiding exists.

The recent development of the theory of topology in the energy bands of crystals [10–46] has created new opportunities for exploring non-Abelian braiding of band-crossing points (nodes) in reciprocal space [47–52], providing an alternative to the real-space braiding exploited by other strategies. Real-space braiding is practically constrained to boundary states,

which has made experimental observation and manipulation difficult; instead, reciprocal-space braiding occurs in the bulk states of the band structures and we demonstrate in this work that this provides a straightforward platform for non-Abelian braiding. Concretely, reciprocal-space braiding occurs between nodes carrying non-Abelian frame charges in multiband systems described by a real Hamiltonian [48–60], and as such is referred to as *multigap topology*, in contrast to the single-gap topology associated with two-band systems. The real Hamiltonian constraint leads to a real basis of eigenvectors [48–54,61,62] and is fulfilled with the symmetry requirement of either (i) a combination of C_2 rotation symmetry and time-reversal symmetry T for both spinful and spinless systems, or (ii) a combination of spatial inversion symmetry P and time-reversal symmetry T for spinless systems. In any multiband system arising from a real Hamiltonian, the band-crossing points carry non-Abelian frame charges that can be converted through the braiding of nodes belonging to adjacent energy gaps [51,53,54,63]. If a pair of nodes within a gap carry the same frame charge (with the same sign), they cannot be annihilated when brought together. Conversely, two nodes within the same gap with opposite frame charges can be annihilated. When nodes are braided, the signs of their non-Abelian frame charges flip, thus changing the relative stability between pairs of nodes in the same gap. As a consequence, the braiding of nodes is accompanied with the transfer of stable pairs of nodes from one gap to an adjacent gap.

To achieve elementary braiding it is necessary to braid one node of an energy gap with a node of an adjacent gap (the gap immediately above or immediately below in energy). The motion of the nodes can be driven by modifying the band structure of the material with the application of external

stimuli. In solid-state systems, where the band structure inherits the symmetries of the crystal, braiding involves groups of nodes that are related by symmetry. Moreover, the braid trajectories usually collapse onto the high-symmetry points of the Brillouin zone. As a consequence, the transfer of a stable pair of nodes from one gap to an adjacent gap is often manifested by a band inversion at one of the high-symmetry points, and such band inversion provides a very direct signature of the braiding process in crystalline systems. This phenomenology is rather general, and reciprocal-space braiding can in principle occur in multiband systems of *any* quasiparticle, including electrons and phonons.

In this work we argue that phonons are an ideal platform to study the non-Abelian braiding of band nodes in the context of multigap topology. As a bosonic excitation associated with ionic vibrations, the entire phonon spectrum is readily accessible to external probes. This contrasts with fermionic excitations such as electrons, in which the Pauli exclusion principle means that only band nodes near the Fermi level can be accessed, placing significant restrictions to the full exploitation of multigap topologies. Additionally, phonons are charge neutral, spinless quasiparticles, and time-reversal symmetry T is hard to break in phonons because they do not directly couple to magnetic fields. For these reasons, the symmetry requirements of real Hamiltonians can be easily fulfilled by phonons in a wide range of materials, suggesting that many will exhibit non-Abelian frame charges in their phonon dispersion. This motivates us to extend the study of phonon bands from single-gap topologies, which have been extensively studied [64–83], to multigap topologies, which remain largely unexplored.

The main purpose of our work is to provide a general framework to study non-Abelian braiding of phonons using first-principles methods, enabling the accurate material-specific calculation of multigap topologies in the phonon bands of any material. The key mathematical objects to study multigap topologies are (i) non-Abelian frame charges, and (ii) a topological invariant called *Euler class*, which captures the relative stability of a pair of nodes within the same gap, that is, whether annihilation of the nodes is possible or not, and that in turn depends on their trajectory with respect to the nodes of the adjacent gaps. We describe the calculation of the Euler class for phonon bands using the phonon eigenvectors that can be obtained from a first-principles lattice dynamics calculation. We also explain how to then use the Euler class to derive the global topological configurations of all the nodes in the multiband system.

To illustrate our method, we study non-Abelian braiding of phonons in monolayer Al_2O_3 from first principles. We show that Al_2O_3, a well-known dielectric material, carries non-Abelian frame charges in its phonon dispersion, and that braiding within a three-band subspace can be driven with electrostatic doping. We explain in detail how to determine the Euler class to construct consistent topological configurations during the braiding process, thus providing a template for analogous calculations in other materials. Our main prediction, non-Abelian braiding constrained by crystal symmetry and driven by electrostatic doping in monolayer Al_2O_3, constitutes a robust proposal for the practical realization of this phenomenon. Additionally, Al_2O_3 has been widely

incorporated into electronic devices as a dielectric material [84–87] and, as a result, electrostatic doping using a gate voltage could be seamlessly integrated into the modern microelectronics industry.

The paper is structured as follows. In Sec. II, we review the theoretical background behind non-Abelian frame charges, the associated patch Euler class, and the Dirac strings that connect nodes with half-integer Euler class [48]. We then present a general computational methodology to calculate the Euler class of phonon band-crossing points from first principles in Sec. III. In Sec. IV, we apply this methodology to study non-Abelian braiding of phonons driven by electrostatic doping in monolayer Al_2O_3 taking place in a three-band subspace. In Sec. V, we present our conclusions and discuss future research directions.

II. THEORETICAL BACKGROUND

A. Non-Abelian frame charges

We start by introducing non-Abelian frame charges in the context of a three-band Bloch Hamiltonian of a two-dimensional system with C_2T symmetry. The spectral decomposition of the 3×3 Hamiltonian gives

$$H = \sum_{n=1,2,3} |e_n\rangle E_n \langle e_n|, \tag{1}$$

with the ordered eigenvalues $E_1 < E_2 < E_3$ (which we assume to be gapped) and the eigenvectors $\{|e_n\rangle\}_{n=1,2,3}$ that can be chosen to be real in an appropriate basis [50]. As a result, the three real and normalized eigenvectors form a three-dimensional orthonormal frame $(|e_1\rangle, |e_2\rangle, |e_3\rangle) \in \mathbb{R}^3 \times \mathbb{R}^3$, that is, an orthogonal matrix O(3) or, fixing the handedness (i.e.. the orientation of the frame), a 3D rotation matrix SO(3). For real eigenvectors, the gauge phase degree of freedom of complex eigenvectors turns into a $+/-$ sign degree of freedom [50,54]; specifically, $(|e_1\rangle, |e_2\rangle, |e_3\rangle), (|e_1\rangle, -|e_2\rangle, -|e_3\rangle), (-|e_1\rangle, |e_2\rangle, -|e_3\rangle)$, and $(-|e_1\rangle, -|e_2\rangle, |e_3\rangle)$ all represent the same state (the orientation of the frame is not preserved if only one sign flips). Therefore, the order-parameter space of the Hamiltonian can be expressed as SO(3) modulo the group of π rotations that flip the sign of two eigenvectors, namely, SO(3)/D$_2$ (the dihedral point group D$_2 = \{E, C_2, C_2', C_2''\}$ is composed of three independent and perpendicular π rotations) [63].

For a band-crossing point (node) in a three-band system, we can define a topological frame charge by the geometry of the SO(3) rotations encircling the node in momentum space, as the acquired angle can be calculated by decomposing the three-dimensional (3D) rotation matrix around the encircled node [50,51,54,88]. A closed path in SO(3)/D$_2$ can be characterized by the fundamental homotopy group $\pi_1[SO(3)/D_2] = \mathbb{Q}$, where $\mathbb{Q} = (\pm i, \pm j, \pm k, -1, +1)$ is the quaternion group with $i^2 = j^2 = k^2 = -1$, $ij = k$, $jk = i$, $ki = j$, and where the charges $\{i, j, k\}$ anticommute [54]. Lifting the SO(3) frame in the covering spin group Spin(3) = SU(2) and using the correspondence $(-i\sigma_x, -i\sigma_y, -i\sigma_z) \mapsto (i, k, j)$ from the parallel-transported spin frames over a base loop l and the quaternion charges, we can assign a quaternion frame charge to any node formed by the bands within the region bounded by
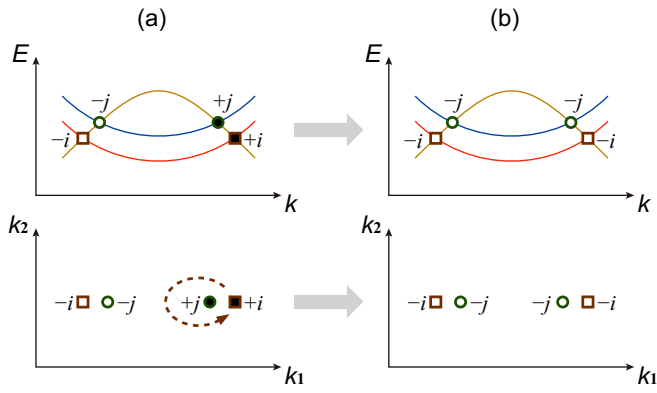
FIG. 1. Topological configurations (a) before and (b) after the braiding. Squares (circles) represent the nodes formed by the lower (upper) two bands, and open (closed) symbols represent the nodes with negative (positive) frame charges. Importantly, the frame charges of the nodes are unambiguously defined only once a base point, an oriented base loop, and choice of gauge have been fixed. We implicitly assume that these have been fixed and we do not show them in the figure.

the loop l [54]. The nodes formed by the lower two bands can thus be characterized by the frame charge $\pm i$, and the nodes formed by the upper two bands can be characterized by $\pm j$. A pair of nodes, one formed by the lower two bands and the other formed by the upper two bands, can be denoted by $\pm k$ as $k = ij$. We note that the sign of the charges is fixed by (i) the gauge chosen for the frame at a base point of the loop, and (ii) the orientation of the parallel transport over the base loop. The stability of a pair of nodes formed by the same two bands can then be characterized by -1 because two nodes with the same frame charge cannot annihilate when brought together, as can be deduced from the algebra of the quaternion charges, i.e., $i^2 = j^2 = k^2 = -1$ [note $k^2 = i \cdot j \cdot i \cdot j = i \cdot j \cdot (-j) \cdot i = i^2 = -1$]. We also conclude that the -1 frame charge is gauge invariant since $(+i)^2 = (-i)^2$, and similarly for j and k. On the other hand, two nodes with opposite frame charges can be annihilated or created pairwise, with a total frame charge of $(-i)(+i) = (-j)(+j) = +1$.

The quaternion group is non-Abelian, as captured by the noncommutativity of the charges $\{i, j, k\}$ and the nontrivial action of their conjugation, e.g., $j^{-1}ij = -jij = j^2i = -i$. This indicates the possibility of flipping the non-Abelian frame charge of a node. Keeping in mind that the frame charges are defined for a fixed base point with a fixed oriented base loop, we can easily see, through the composition of oriented loops, that a conjugation operation, say $j^{-1}ij = -i$, corresponds to the braiding of a node i around a node in an adjacent gap j [54]. Therefore, the band nodes in three-band systems can carry a non-Abelian charge, and the sign of the topological frame charge can be flipped by a braiding processes, as schematically shown in Fig. 1. Hereafter, we use open (closed) symbols to represent the nodes with negative (positive) frame charges. Different from the topological invariants formed only by two bands in single-gap topologies, in three-band systems the frame charge depends on the braiding of the nodes formed by both the lower two and the upper two bands, which involve all three bands [47]. For clarity, we use

squares (circles) to represent the nodes formed by the lower (upper) two bands. As shown in Fig. 1(a), a node formed by the lower two bands with a frame charge $+i$ (labeled as a closed square) can circle another node formed by the upper two bands with a frame charge $+j$ (labeled as a closed circle), and as a result, the signs of the frame charges are changed to be $-i$ and $-j$, respectively [labeled as an open square and an open circle in Fig. 1(b)]. With this process we can create an obstruction to annihilate two opposite nodes, e.g., $+i$ and $-i$ in Fig. 1(a), by braiding one node around another node formed by the neighboring bands, so the frame charges of the pair of nodes become the same, e.g., the two nodes with the same frame charge of $-i$ in Fig. 1(b).

While the quaternion charges intrinsically unveil the non-Abelian nature of the multigap topology of systems described by a real Hamiltonian, they are cumbersome to use in real material band structures because crystal point group symmetries lead to node multiplicities. Fortunately, there exists a complementary quasi-two-dimensional topological invariant which not only simplifies the computation of the topological charges, but also greatly refines the characterization of the topological stability of nodes belonging to the same gap. This is the patch Euler class that we introduce next.

B. Patch Euler class

In the following, we number the bands from lower to higher energy with $E_n \leqslant E_{n+1}$, and we label the partial gap between two successive bands n and $(n + 1)$ as $\{\Delta_n\}$ with $E_n \leqslant \Delta_n \leqslant E_{n+1}$. Similar to the Berry curvature in single-gap topologies, we can compute the Euler curvature (Euler form) for bands n and $(n + 1)$ in gap Δ_n [48,50,58]:

$$\mathrm{Eu}_n(\mathbf{k}) = \langle \partial_{k_1} e_n | \partial_{k_2} e_{n+1} \rangle - \langle \partial_{k_2} e_n | \partial_{k_1} e_{n+1} \rangle, \quad (2)$$

where $|e_n\rangle$ and $|e_{n+1}\rangle$ are eigenvectors of band n and $(n + 1)$, respectively, and $\mathbf{k} = (k_1, k_2)$ are the coordinates of the Brillouin zone. The Euler class χ_n for the bands n and $(n + 1)$ over a patch $\mathcal{D}$ of the Brillouin zone (assuming that there is no node connecting the bands n and $(n + 1)$ to other bands on $\mathcal{D}$) is then defined by [48,50]

$$\chi_n[\mathcal{D}] = \frac{1}{2\pi} \left[\int_{\mathcal{D}} \mathrm{Eu}_n(\mathbf{k}) dk_1 dk_2 - \oint_{\partial \mathcal{D}} \mathbf{a}_n \cdot d\mathbf{k} \right], \quad (3)$$

where $\partial \mathcal{D}$ is the boundary of the patch, and with the Euler connection $\mathbf{a}_{n,i} = \langle e_n | \partial_{k_i} | e_{n+1} \rangle$ for $i = 1, 2$.

When integrated over the whole Brillouin zone, the Euler class χ_n is an integer $\mathbb{Z}$ [47,48,53,89,90], and indicates the presence of $|\chi_n|$ pairs of stable nodes formed by a two-band subspace. When integrated over a patch $\mathcal{D}$, the Euler class in Eq. (3) can either have integer or half-integer values, indicating the presence of $2|\chi_n|$ stable nodes within the patch. For instance, assuming the presence of two nodes within the patch, a Euler class of 0 indicates that the nodes can annihilate [Fig. 2(a)], whereas a Euler class of ± 1 means that they cannot annihilate when brought together [Fig. 2(b)]. Importantly, the Euler class is related to the frame charges discussed above: for a patch containing only one node, a patch Euler class of $\chi_1 = \pm \frac{1}{2}$ ($\chi_2 = \pm \frac{1}{2}$) can be associated to the frame charge $\pm i$ ($\pm j$) and such node is referred to as a linear node [Fig. 2(c)], while the value $|\chi_n| = 1$ indicates the frame
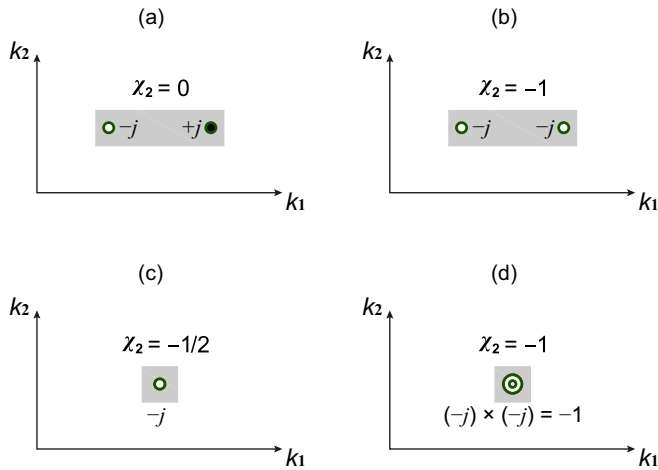
FIG. 2. Patch Euler class for two nodes in the same gap Δ_2 (a) with the opposite frame charges and (b) with the same frame charges, as well as the patch Euler class for (c) a linear node and (d) a quadratic node. We use open (closed) symbols to represent the nodes with negative (positive) frame charges, and one symbol (two concentric symbols) to represent the linear (quadratic) node.

charge -1 and such node is referred to as a quadratic node [Fig. 2(d)]. Hereafter, we label a quadratic node of $|\chi_n| = 1$ as two concentric symbols since it can be interpreted as the superposition of two linear nodes.

We note that the Euler class refines the topological analysis since, contrary to the frame charges, it keeps track of the stability of an arbitrary number of nodes formed by two bands, taking a half-integer (integer) value for an odd (even) number of stable nodes. However, we also note that this requires that the two bands under consideration must be disconnected from all the other bands over the patch. The direct computation of the frame charges remains useful when more than two bands are degenerate at a single point, which can happen at critical points during a band inversion (or in systems with three-dimensional irreducible representations protected by cubic point groups).

One interesting feature of the Euler class is that it gives the lower bound of the powerlike dispersion of the bands at a band crossing [55,58]. More precisely, the number $2|\chi_n|$ gives the lower bound of the exponent of the leading term in a Taylor expansion of the energy eigenvalues at the band crossing. At this stage, a clarification is necessary to distinguish between electrons and phonons. In electronic band structures, the dispersion at band crossings almost always realizes the lower bound indicated by their Euler class because of the strong electrostatic screening provided by electrons. By contrast, and as described below, the frequencies of the phonon bands correspond to the square root of the eigenvalues of the dynamical matrix that defines the topology. Interestingly, the order of band crossings in phonon band structures is almost always doubled, with the exception of the dispersion of the acoustic bands at Γ corresponding to the Goldstone modes of the system [57].

Because the gauge sign (± 1) of the real eigenvectors is not fixed, the absolute sign of the topological charges is not uniquely defined. For example, if we flip the gauge signs of

the orthonormal frame of eigenvectors from $(|e_1\rangle, |e_2\rangle, |e_3\rangle)$ to $(|e_1\rangle, -|e_2\rangle, -|e_3\rangle)$, the sign of the patch Euler class χ_2 also flips, and similarly for the frame charges. Therefore, the sign of the Euler class and of the non-Abelian frame charge is gauge dependent, and for an individual node taken in isolation this sign has no physical meaning. However, the relative sign between two distinct nodes is not gauge dependent as it provides information on the stability of the nodes. Therefore, we can compute the Euler class for different patches, and assign the sign of the topological frame charges to get a consistent global topological configuration where the relative signs of all nodes agree with their gauge-invariant relative stability. Such a global picture can be obtained by fixing the gauge globally [58]. For this, we introduce in Sec. II C the last conceptual object that is needed, namely, the Dirac string [48].

C. Dirac strings

If we consider two linear nodes in gap Δ_n, each band eigenvector forming the nodes $\{|e_n\rangle, |e_{n+1}\rangle\}$ carries a π Berry phase on any loop encircling one node at the time, thus indicating a π disclination line connecting the two nodes. The gauge sign of the eigenvectors must then flip when crossing this line [89]. We can use a Dirac string to visualize the line connecting the two nodes, in analogy with the Dirac string connecting two Weyl nodes in 3D indicating the winding of the U(1) gauge phase of complex eigenvectors.

The trajectory of the Dirac string is not unique because we can change the gauge signs of the eigenvectors (although such local change do not affect the topological stability of whether any pair of nodes can be annihilated when merged). Despite the fact that we can assign different Dirac strings for the same pair of nodes, the trajectory of a Dirac string between two nodes is constrained by the gauge freedoms of all other nodes, collectively leading to what are known as the "Dirac string rules" [48,55]:

(1) All linear nodes formed by the same two bands must be connected by Dirac strings in pairs, whereas the quadratic nodes can be interpreted as two linear nodes merged together with an internal Dirac string.

(2) The sign of the frame charge of a node in Δ_n changes when crossing a Dirac string connecting two nodes in the neighboring gaps (Δ_{n-1} or Δ_{n+1}). This can be realized either by moving the node in Δ_n across a fixed Dirac string in Δ_{n-1} or Δ_{n+1} [Fig. 3(a)] or by moving a Dirac string in the neighboring gap across the fixed node [Fig. 3(b)].

(3) All the Dirac strings connecting the nodes in the same gap can be reassigned by changing their start and end nodes. For example, in Fig. 4 we can connect node 1 with node 3 and node 2 with node 4, or connect node 1 with node 2 and node 3 with node 4, or connect node 1 with node 4 and node 2 with node 3.

By systematically computing the Euler class of every single band crossing, and then of every pair of band crossings in the same gap, we can assign a signed frame charge to every node, as well as the Dirac strings that connect every pair of linear nodes, such that we obtain a consistent global topological configuration [55,58], as discussed in the next subsection. This procedure works like a puzzle: we arbitrarily fix the sign, i.e., the gauge, of an initial node and then we iteratively assign
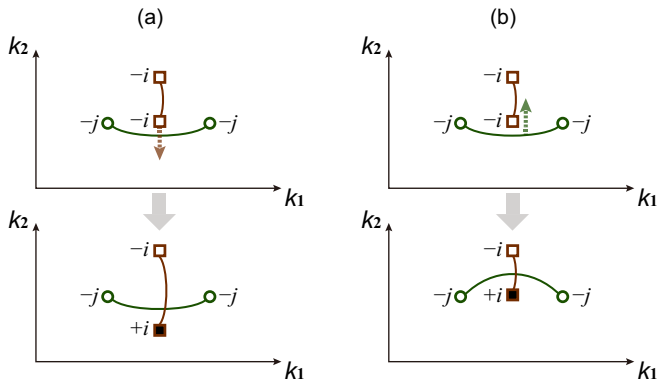
FIG. 3. Flipping of the sign of the frame charge by (a) moving the node across a fixed Dirac string or (b) moving a Dirac string across the fixed node. We note that these processes amount to the same thing.

the Dirac strings of the neighboring nodes in a consistent manner, i.e., under the constraint of the gauge-invariant values of all the patch Euler classes previously computed.

D. Global topological configuration

To obtain the global topological configuration, we start by dividing the Brillouin zone into different patches, each containing a pair of nodes in the same gap, and the patches cover all the nodes. We then calculate the Euler class for each patch, which provides information on the relative stability within each and every pair of the nodes.

We then specify the relative signs of the frame charges for all the nodes based on the patch Euler class calculations, and afterwards connect all the linear nodes in pairs by Dirac strings to make the Euler class for all the patches consistent with each other. Even within each patch there are two possible configurations: a patch Euler class of ± 1 (0) can either correspond to two nodes with the same (opposite) frame charge(s), or contain two opposite (same) charge nodes and an extra Dirac string in the neighboring gap.

We next check whether the assignment of frame charges and Dirac strings is physically consistent for the global topological configuration. As long as the frame charges and the Dirac string of one patch are fixed, the rest of the global topological configuration can be deduced like a puzzle based on the computed Euler class for all the patches and the Dirac string rules.

Because the local gauge sign is not fixed, the start and end nodes of the Dirac strings, as well as the corresponding trajectory, are not unique. Therefore, for a given set of patch
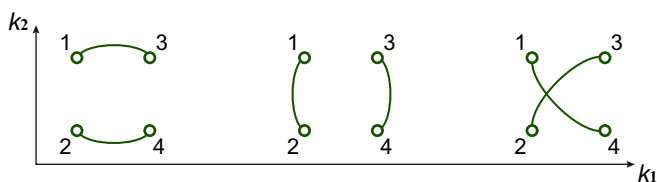

FIG. 4. Dirac strings reassigned by changing the start and end nodes.

Euler classes, there may be many different (but consistent) global topological configurations. The difference comes from the local and global gauge choices. However, the different global topological configurations capture the same physics, for example, whether a pair of nodes will annihilate or not, which is gauge invariant.

We can apply the same strategy, based on the calculated Euler class and the Dirac string rules, to obtain the topological configurations during the braiding processes that take place when the system undergoes a transformation of its band structure, i.e., during a topological phase transition upon band inversion. However, once the global topological configuration of the system is known, the topological configuration of any other phases reached upon the displacement of the nodes and band inversions can be readily predicted by applying the conversion rules presented above.

In real materials, where the crystal symmetries constrain the movement of the nodes and often collapse the braid trajectories to the high-symmetry points, these rules need to be complemented with the crystal symmetry rules contained in the irreducible representations which dictate when a band crossing can be avoided or not. These concepts are exemplified in Sec. IV, which describes the braiding of phonons in aluminum oxide.

Overall, this establishes a theoretical framework to study non-Abelian braiding of *any quasiparticle* with three bands in their spectra, as long as the system has $C_2 T$ symmetry so that the corresponding Hamiltonian is real [50]. We refer the reader to Refs. [47,50,54,89] and especially Ref. [58] for more details. The theoretical formalism we have described can also be extended to spinless systems of any dimensions with PT symmetry.

III. COMPUTATIONAL METHODOLOGY

The key quantity in the theoretical formalism described in the previous section is the Euler form in Eq. (2). Its evaluation requires the eigenvectors of the quasiparticles as input, and these eigenvectors can be directly calculated from first principles for a range of quasiparticles. In this work, we use phonons as an example quasiparticle to describe how to calculate the patch Euler class. As discussed earlier, we focus on phonons because (i) their bosonic nature means the entire spectrum is accessible (in contrast to the restriction to the Fermi energy in fermionic systems), and (ii) the time-reversal symmetry T is hard to break in phononic systems.

A. Lattice dynamics

The ions in solids vibrate around their equilibrium positions $\mathbf{r}(l\kappa)$ with displacements $\mathbf{u}(l\kappa)$, where l and κ label the unit cells and the atoms in each unit cell, respectively. Under the harmonic approximation, the potential energy surface can be expressed as a quadratic function of the displacements of the atoms [91,92]

$$\Phi = \Phi_0 + \frac{1}{2} \sum_{ll'\kappa\kappa'} \sum_{\alpha\beta} \Phi_{\alpha\beta}(l\kappa, l'\kappa') u_\alpha(l\kappa) u_\beta(l'\kappa'), \quad (4)$$

where α and β are the Cartesian indices, Φ_0 is the zeroth-order force constant evaluated at the ionic equilibrium positions,

and $\Phi_{\alpha\beta}(l\kappa, l'\kappa')$ are the second-order force constants which can be evaluated as the second derivatives of Φ with respect to ionic displacements, or equivalently as the first derivatives of the atomic force on atom $l'\kappa'$ under an atomic displacement $\mathbf{u}(l\kappa)$ [92,93]:

$$\Phi_{\alpha\beta}(l\kappa, l'\kappa') = \frac{\partial^2 \Phi}{\partial u_\alpha(l\kappa)\partial u_\beta(l'\kappa')} = -\frac{\partial F_\beta(l'\kappa')}{\partial u_\alpha(l\kappa)}. \quad (5)$$

This can be calculated using the finite-differences method [94–96] or using density functional perturbation theory [97].

The dynamical properties of the ionic motion are then determined by the dynamical matrix $D(\mathbf{q})$, which plays the role of the Hamiltonian, and is obtained from the second-order force constants as [98–100]

$$D_{\kappa\kappa'}^{\alpha\beta}(\mathbf{q}) = \sum_{l'} \frac{\Phi_{\alpha\beta}(0\kappa, l'\kappa')}{\sqrt{m_\kappa m_{\kappa'}}} e^{i\mathbf{q}\cdot[\mathbf{r}(l'\kappa') - \mathbf{r}(0\kappa)]}, \quad (6)$$

where $\mathbf{q}$ is the wave vector and m_κ is the mass of atom κ. The eigenvalue equation of the Hamiltonian (dynamical matrix) is then

$$\sum_{\beta\kappa'} D_{\kappa\kappa'}^{\alpha\beta}(\mathbf{q}) e_{\mathbf{q}n}^{\beta\kappa'} = \omega_{\mathbf{q}n}^2 e_{\mathbf{q}n}^{\alpha\kappa}, \quad (7)$$

where n is the band index, $\omega_{\mathbf{q}n}$ are the phonon frequencies, and $e_{\mathbf{q}n}^{\alpha\kappa}$ are the phonon eigenvectors in matrix form.

The dynamical matrix $D(\mathbf{q})$ is a $3N \times 3N$ matrix, where 3 comes from the three Cartesian directions and N is the number of atoms in the unit cell. As a result, the eigenvectors $\mathbf{e}_{\mathbf{q}n}$, which are needed to evaluate the Euler form, are complex column vectors with $3N$ elements

$$\mathbf{e}_{\mathbf{q}n} = \begin{pmatrix} e_{\mathbf{q}n}^{x1} \\ e_{\mathbf{q}n}^{y1} \\ e_{\mathbf{q}n}^{z1} \\ \vdots \\ e_{\mathbf{q}n}^{xN} \\ e_{\mathbf{q}n}^{yN} \\ e_{\mathbf{q}n}^{zN} \end{pmatrix}, \quad (8)$$

and can be normalized to 1:

$$\sum_{\alpha\kappa} \left| e_{\mathbf{q}n}^{\alpha\kappa} \right|^2 = 1. \quad (9)$$

We also note that we use the conventional label $\mathbf{q}$ to describe coordinates in the phonon Brillouin zone, rather than the general label $\mathbf{k}$ used in Sec. II.

The phonon eigenvectors can be used to obtain the associated atomic displacements [92,93,98]

$$[\mathbf{u}(l1), \ldots, \mathbf{u}(lN)] = \left[\frac{A}{\sqrt{m_1}} \mathbf{e}_{\mathbf{q}n}^1 e^{i\mathbf{q}\cdot\mathbf{r}(l1)}, \ldots, \frac{A}{\sqrt{m_N}} \mathbf{e}_{\mathbf{q}n}^N e^{i\mathbf{q}\cdot\mathbf{r}(lN)} \right], \quad (10)$$

where the three-component vectors $\mathbf{e}_{\mathbf{q}n}^\kappa = (e_{\mathbf{q}n}^{x\kappa}, e_{\mathbf{q}n}^{y\kappa}, e_{\mathbf{q}n}^{z\kappa})$, and A is the complex constant [92,93,98].

B. Euler class calculations

After obtaining the phonon dispersion and eigenvectors, we need to find all the phonon band-crossing points in gap Δ_n. Then we divide the 2D Brillouin zone into different patches, and each patch contains either one node or a pair of nodes in Δ_n. The phonon eigenvectors $\mathbf{e}_{\mathbf{q}n}$ and $\mathbf{e}_{\mathbf{q}(n+1)}$ are computed on a discretized grid over the patch. We clarify that the patch for nodes in Δ_n should not overlap with the positions of nodes in the neighboring gaps Δ_{n-1} and Δ_{n+1}.

The Euler form in Eq. (2) is calculated for all the patches in gap Δ_n with the phonon eigenvectors $\mathbf{e}_{\mathbf{q}n}$ and $\mathbf{e}_{\mathbf{q}(n+1)}$ as input. For each band and $\mathbf{q}$ point, the eigenvector is generally composed of a set of three complex values associated with each atom along the Cartesian axes. In the presence of C_2T symmetry (or PT symmetry) that squares to the identity, there always exists a unitary transformation under which the dynamical matrix becomes real, and the associated eigenvectors are then also real. This unitary transformation is obtained through the Takagi factorization of the matrix representation of the C_2T symmetry, which turns out to be symmetric [50]. Then, isolating the unitary part of the matrix representation of C_2T, the Takagi factorization can be readily obtained through singular-value decomposition [59,101]. We provide an explicit example of this procedure in Sec. IV B below for aluminum oxide.

Using the real basis we can directly evaluate the expression in Eq. (3), which is implemented in a publicly available *Mathematica* code [102]. Alternatively, we note that the patch Euler class of nodes can be calculated by employing Wilson-loop methods [50,53]. Because of the random sign gauge $+/-$ and the presence of the Dirac string with a gauge transformation, we can smooth the eigenvectors by computing the Berry phase and fixing the position of the Dirac strings. As a result, the eigenvectors $\mathbf{e}_{\mathbf{q}n}$ and $\mathbf{e}_{\mathbf{q}(n+1)}$ vary smoothly away from the Dirac strings, with both states flipping their signs simultaneously when crossing a Dirac string. The Berry phase calculations also provide information on the positions and the Berry curvature of the nodes, which helps to verify whether the patch contains the node(s) we are interested in. For details we refer the reader to the Supplemental Material of Ref. [50]. The gauged eigenvectors can then be used to compute Eq. (3) over the patch $\mathcal{D}$.

After evaluating the relative stability of each pair of nodes, we can assign the frame charges to all the nodes based on the Euler class of all the patches, as well as the Dirac strings that connect all the linear nodes. We repeat this procedure until a global topological configuration is obtained, as outlined above.

IV. CASE STUDY: PHONON BRAIDING IN MONOLAYER Al$_2$O$_3$

In this section, we exemplify the calculation of the Euler class and associated non-Abelian braiding using first-principles methods. To do so, we explore non-Abelian braiding in the phonon spectrum of monolayer Al$_2$O$_3$ as controlled by electrostatic doping.

A. First-principles calculations

Density functional theory (DFT) calculations are performed with the Vienna *ab initio* simulation package (VASP) [103,104]. The generalized gradient approximation (GGA) with the Perdew-Burke-Ernzerhof (PBE) parametrization is used as the exchange-correlation functional [105]. A plane-wave basis with a kinetic energy cutoff of 800 eV and a 9×9 **k** mesh are used for monolayer Al_2O_3. The self-consistent field calculations are stopped when the energy difference between successive steps is below 10^{-6} eV, and the structural relaxation is stopped when forces are below 10^{-3} eV/Å. A vacuum spacing larger than 20 Å is used to eliminate interactions between adjacent layers. Electrostatic doping is simulated by introducing extra charges with a compensating background. There is no out-of-plane dipole upon electrostatic doping as the extra charge is distributed evenly on the 2D plane [106]. We keep the lattice constants fixed upon doping to mimic the material growth on a substrate, and the ionic positions remain the same upon doping under structural relaxation.

The force constants to determine the phonons are computed using the finite-differences method in a 3×3 supercell (equivalent to a 3×3 phonon **q** mesh) with a 3×3 electronic **k** mesh using VASP. The phonon dispersion and phonon eigenvectors are obtained using PHONOPY [92,93]. Convergence tests have been performed comparing supercells of sizes between 3×3 and 6×6 [106]. We also check the convergence of the phonon dispersion in doped Al_2O_3 with respect to the vacuum spacing, which shows that the phonon frequencies are independent of the vacuum spacing [106]. This is consistent with the fact that no out-of-plane dipole is observed upon doping, and it is therefore sufficient to use the compensating background charge when introducing the extra charges, without the need to include a Coulomb cutoff in the vacuum spacing [107]. We focus on hole doping because imaginary phonon modes are observed upon electron doping, indicating that the lattice becomes dynamically unstable in the latter case [106]. The splitting between the longitudinal and transverse optical phonons (LO-TO splitting) is neglected because in 2D materials no LO-TO splitting occurs at Γ and only the slope of phonon bands changes [108], which implies that the nodal structure will remain unchanged.

The phonon band-crossing points for all the bands are calculated using WANNIERTOOLS [109]. After obtaining all the nodes in gap Δ_n, we divide the 2D Brillouin zone into different patches, and each patch contains either one node or a pair of nodes in Δ_n. Each patch in the 2D Brillouin zone is sampled with a 30×30 **q** mesh, and the phonon eigenvectors $\mathbf{e}_{\mathbf{q}n}$ and $\mathbf{e}_{\mathbf{q}(n+1)}$ are computed at each of the points sampled, and subsequently rotated to the real basis. The real eigenvectors are then used to calculate the patch Euler class using a modified version of a publicly available *Mathematica* code [102], with the calculated real eigenvectors as input.

B. C_2T representation and Takagi factorization

In this section we detail the steps to transform the phonon eigenvectors to a real basis in the case of monolayer Al_2O_3. This real representation of the eigenvectors is needed to compute the patch Euler class as explained above.

Before deriving the unitary transformation to the real basis, we first need to derive the generic condition on the dynamical matrix that originates from the C_2T symmetry. For this we use the action of symmetries on the displacements $\mathbf{u}(l\kappa) = [u_x(l\kappa), u_y(l\kappa), u_z(l\kappa)]$ at a given unit cell l and a given atomic site κ within the unit cell, i.e., for $\kappa \in \{1, 2, 3, 4, 5\} \equiv \{Al_1, Al_2, O_1, O_2, O_3\}$. It will be convenient to use the ket-form of the displacement vectors

$$\mathbf{u}(l\kappa)^t = [u_x(l\kappa)\, u_y(l\kappa)\, u_z(l\kappa)]. \tag{11}$$

Since the system here has both C_2 (rotation by π around the $\hat{z}$ axis) and T (time-reversal) symmetries, we consider the action of each symmetry separately. The action of C_2 on the displacements gives

$$^{C_2}\mathbf{u}(l\kappa)^t = \mathbf{u}(C_2[l\kappa])^t \cdot \Gamma^{(\text{vec})}(C_2), \tag{12}$$

where $\Gamma^{(\text{vec})}(C_2)$ is the vector representation of the point group of the system for C_2, i.e.,

$$\Gamma^{(\text{vec})}(C_{2z}) = \text{diag}(-1, -1, 1), \tag{13}$$

while $C_2[l\kappa]$ stands for

$$C_2\mathbf{r}(l\kappa) = \mathbf{r}(l'\kappa') = \mathbf{r}(l\kappa') + \mathbf{\Delta}_{ll'}, \tag{14}$$

where $\mathbf{\Delta}_{ll'} = \mathbf{R}_{l'} - \mathbf{R}_l$ is a Bravais vector and $\mathbf{r}(l\kappa')$ is the position of the κ'th atomic site within the lth unit cell determined through the permutation

$$C_2(Al_1\ Al_2\ O_1\ O_2\ O_3) = (Al_1\ Al_2\ O_1\ O_2\ O_3) \cdot U_{\text{perm}}$$
$$= (Al_2\ Al_1\ O_1\ O_2\ O_3), \tag{15}$$

where $U_{\text{perm}} = \sigma_x \oplus \mathbb{1}_3$. The action of T simply gives

$$^T\mathbf{u}(l\kappa)^t = \mathcal{K}\mathbf{u}(l\kappa)^t = \mathbf{u}(l\kappa)^t\mathcal{K}, \tag{16}$$

where $\mathcal{K}$ is the complex conjugation, and the last equality follows from the assumption that the displacements are real. Let us now rewrite the displacement in the Bloch form

$$\mathbf{u}(l\kappa) = \sum_{\mathbf{q}\in\text{BZ}} e^{i\mathbf{q}\cdot\mathbf{r}(l\kappa)}\boldsymbol{\varepsilon}_{\mathbf{q}}(\kappa) \tag{17}$$

(BZ is the Brillouin zone), through which the potential energy takes the form

$$\sum_{ll'} \mathbf{u}(l\kappa)^t \cdot \mathbf{\Phi}(l\kappa, l'\kappa') \cdot \mathbf{u}(l\kappa)$$
$$\propto \sum_{\mathbf{q}\in\text{BZ}} \boldsymbol{\varepsilon}_{\mathbf{q}}(\kappa)^\dagger \cdot D_{\kappa\kappa'}(\mathbf{q}) \cdot \boldsymbol{\varepsilon}_{\mathbf{q}}(\kappa'), \tag{18}$$

where we have used $\boldsymbol{\varepsilon}_{\mathbf{q}}(\kappa)^* = \boldsymbol{\varepsilon}_{-\mathbf{q}}(\kappa)$ that follows from the reality of $\mathbf{u}(l\kappa)$. Then, we get the C_2T-symmetry constraint on the dynamical matrix from the symmetry action on the Bloch components $\boldsymbol{\varepsilon}_{\mathbf{q}}(\kappa)$.

Ordering the Bloch components into a (1×15) complex vector, i.e.,

$$|\boldsymbol{\varepsilon}_{\mathbf{q}}\rangle = [\varepsilon_{\mathbf{q},x}(1)\, \varepsilon_{\mathbf{q},y}(1)\, \varepsilon_{\mathbf{q},z}(1) \ldots \varepsilon_{\mathbf{q},x}(5)\, \varepsilon_{\mathbf{q},y}(5)\, \varepsilon_{\mathbf{q},z}(5)]^*, \tag{19}$$

the **q** component of the potential energy takes the form

$$|\boldsymbol{\varepsilon}_{\mathbf{q}}\rangle \cdot D(\mathbf{q}) \cdot \langle\boldsymbol{\varepsilon}_{\mathbf{q}}|, \tag{20}$$

and from Eqs. (12)–(16) we get the C_2T-symmetry action

$$^{C_2T}|\boldsymbol{\varepsilon_q}\rangle = |\boldsymbol{\varepsilon}_{-C_2\mathbf{q}}\rangle \cdot U_{C_2T}\mathcal{K} = |\boldsymbol{\varepsilon_q}\rangle \cdot U_{C_2T}\mathcal{K}, \qquad (21)$$

with

$$U_{C_2T} = U_{\text{perm}} \otimes \Gamma^{(\text{vec})}(C_2). \qquad (22)$$

The invariance of the potential energy under C_2T symmetry then gives the following constraint on the dynamical matrix:

$$^{C_2T}(\Phi - \Phi_0) = (\Phi - \Phi_0),$$

$$\Leftrightarrow \quad U_{C_2T} \cdot [D(\mathbf{q})]^* \cdot U_{C_2T}^\dagger = D(\mathbf{q}). \qquad (23)$$

First, we verify that the double action of C_2T gives an identity, i.e.,

$$\langle \boldsymbol{\varepsilon_q}|^{[C_2T]^2}|\boldsymbol{\varepsilon_q}\rangle = U_{C_2T} \cdot (U_{C_2T})^* = \mathbb{1}_{15}. \qquad (24)$$

Then, by unitarity $(U_{C_2T})^* = [(U_{C_2T})^t]^{-1}$, and we readily obtain that the matrix is symmetric, i.e., $U_{C_2T} = (U_{C_2T})^t$. We can therefore perform a Takagi factorization, given by $U_{C_2T} = U_{\text{tf}} \cdot \Lambda \cdot (U_{\text{tf}})^t$ where Λ is diagonal, from which we define the unitary matrix $W = \sqrt{\Lambda^*} \cdot (U_{\text{tf}})^\dagger$. We describe below how to derive the unitary matrices Λ and U_{tf}.

We now define the rotated basis $\widetilde{\boldsymbol{\varepsilon}}$ through

$$|\boldsymbol{\varepsilon_q}\rangle = |\widetilde{\boldsymbol{\varepsilon}}_\mathbf{q}\rangle \cdot W, \qquad (25)$$

in which the dynamical matrix is real. Indeed, the representation of C_2T in the new basis reads as

$$^{C_2T}|\widetilde{\boldsymbol{\varepsilon}}_\mathbf{q}\rangle = |\widetilde{\boldsymbol{\varepsilon}}_\mathbf{q}\rangle \cdot (WU_{C_2T}W^t)\mathcal{K} = |\widetilde{\boldsymbol{\varepsilon}}_\mathbf{q}\rangle\mathcal{K}, \qquad (26)$$

i.e., the unitary part of C_2T is now a unit matrix. Rotating the dynamical matrix in the new basis, i.e.,

$$W \cdot D(\mathbf{q}) \cdot W^t = \widetilde{D}(\mathbf{q}), \qquad (27)$$

the C_2T-symmetry constraint (23) becomes

$$[\widetilde{D}(\mathbf{q})]^* = \widetilde{D}(\mathbf{q}). \qquad (28)$$

We conclude that the eigenvectors of $\widetilde{D}(\mathbf{q})$ must be real (and symmetric).

We end with the derivation of W. Because U_{C_2T} is unitary on top of being symmetric, the Takagi factorization is readily given through a singular-value decomposition [101], i.e., $U_{C_2T} = U_{\text{svd}} \cdot \Lambda \cdot V_{\text{svd}}$ with $\Lambda = \mathbb{1}$, from which we get $U_{\text{tf}} = U_{\text{svd}} \cdot \sqrt{(U_{\text{svd}})^\dagger \cdot (V_{\text{svd}})^*}$. The unitary matrix that rotates to the new basis is finally given by $W = (U_{\text{tf}})^\dagger$.

We note that the above derivation is completely general, with only U_{C_2T} being system dependent (for another example of this procedure applied to an electronic band structure problem, see Ref. [59]).

C. Crystal structure and phonon dispersion

Monolayer Al_2O_3 is predicted to crystallize in a honeycomb lattice [110]. The aluminum and oxygen atoms are in the same plane, with the oxygen atoms forming a kagome lattice in 2D, as shown in Fig. 5(a). The calculated lattice constant of 5.842 Å agrees well with previous calculations [110]. Monolayer Al_2O_3 belongs to the $P6/mmm$ space group (No. 191), which has C_2 rotation symmetry. In addition, in phonons the time-reversal symmetry T is automatically satisfied. With C_2T
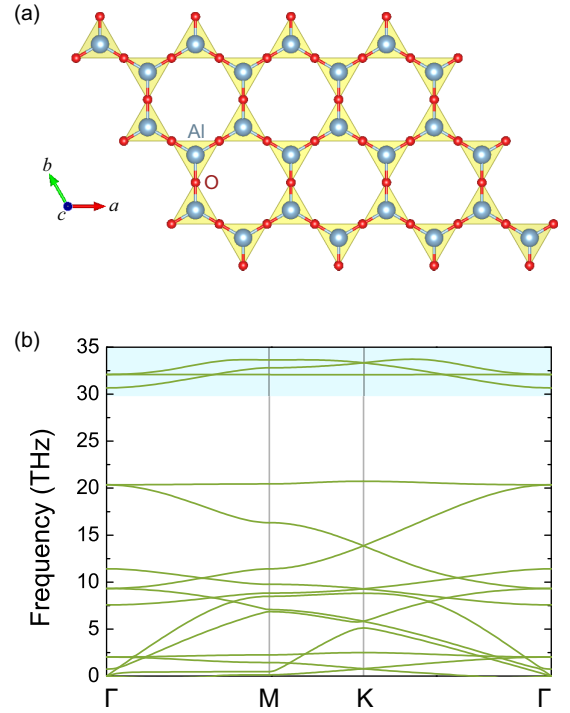
(a)

FIG. 5. (a) Crystal structure and (b) phonon dispersion of monolayer kagome Al_2O_3.

symmetry, phonons in monolayer Al_2O_3 can be described by a real Hamiltonian (dynamical matrix), and consequently we can assign non-Abelian frame charges to different nodes in any three-band subsystem in the entire phonon spectrum.

Figure 5(b) shows the calculated phonon dispersion. No imaginary phonon modes are observed, indicating the dynamical stability of monolayer Al_2O_3. There are 5 atoms in the unit cell, leading to 15 phonon branches. We focus on the top three bands, i.e., bands 13–15 marked in the blue area between 30 and 35 THz in Fig. 5(b), because they are isolated from other phonon bands and are more sensitive to electrostatic doping [106], thus providing an ideal platform to explore multigap topology and non-Abelian braiding.

D. Band inversion upon electrostatic doping

Bulk Al_2O_3 is a well-known dielectric material used in electronic devices. Therefore, electrostatic doping of monolayer Al_2O_3 by gate voltage can be easily incorporated into the existing microelectronics industry. We simulate the phonon spectra of Al_2O_3 upon electrostatic doping. As shown in Fig. 6, the phonon frequencies of bands 13–15 at the Γ point have only slight changes upon doping. On the other hand, the highest phonon bands at the K point with double degeneracy move to much lower frequency with increasing doping concentration, whereas the frequency of the nondegenerate single band at K remains nearly the same. Therefore, the band order at K is inverted at -0.14 $e/\text{f.u.}$, with the double-degenerate band becoming lower than the single band.

Such phonon band inversion redistributes the band nodes in two neighboring gaps Δ_{13} and Δ_{14}, and consequently induces conversions of the frame charges. The transfer of frame
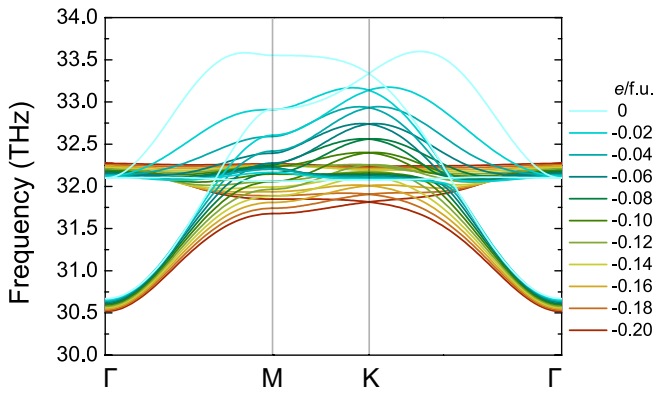
FIG. 6. Evolution of phonon bands 13–15 upon electrostatic doping.

charges between different gaps is accompanied by the non-Abelian braiding of the nodes. It is, however, important to note that the crystalline symmetries of the system constrain the movements of the nodes over the Brillouin zone with, as a consequence, the collapse of the braid trajectories onto the high-symmetry points Γ and K. In the next subsections we first investigate the topological configurations at different doping concentrations individually, and then obtain the complete picture of the braiding processes upon electrostatic doping.

E. Frame charges of undoped Al_2O_3

We first investigate the phonon band-crossing points formed by bands 13, 14, and 15 of undoped Al_2O_3. To be consistent with the notation introduced in the theoretical background section (Sec. II), we use squares to represent single nodes in gap Δ_{13} formed by bands 13 and 14, and circles for single nodes in gap Δ_{14} formed by bands 14 and 15. As shown in Fig. 7(a), a band-crossing point is formed when the two crossing bands belong to different irreducible representations (irreps), whereas two bands with the same irrep remain gapped. To be specific, the violet square node along $\Gamma - M$ formed by bands 13 and 14 [red and blue lines in Fig. 7(a)] is not gapped as the two bands belong to irreps Σ_1 and Σ_2, but these two bands have an avoided crossing along $K - \Gamma$ because in that case they belong to the same irrep Λ_4. In addition, there are two circle nodes at Γ and K formed by bands 14 and 15 [blue and yellow lines in Fig. 7(a)] with 2D irreps Γ_6^- and K_5, respectively.

Figure 7(b) shows the position of all the nodes. We first compute the Euler class for single nodes, as indicated by patches 1–3 in Fig. 7(b). In patch 1, the dark yellow circle at the Γ point has a Euler class of -1, indicating a quadratic node. This agrees well with the quadratic dispersion near Γ. Consistent with Sec. II, we label the quadratic node by a small circle inside a large circle because it can be viewed as two linear nodes merged together. On the other hand, the Euler class for the dark green circle in Δ_{14} at the K point (patch 2) and the violet square in Δ_{13} along the $\Gamma - M$ high-symmetry line (patch 3) is $\pm\frac{1}{2}$, indicating two linear nodes. Note that for a single node the sign of the Euler class has no physical meaning due to the $+/-$ sign freedom, but the relative signs of two nodes in the same gap provide information on their
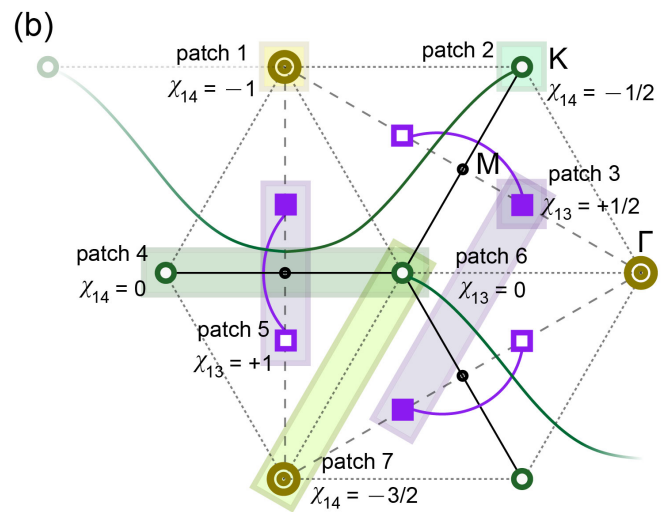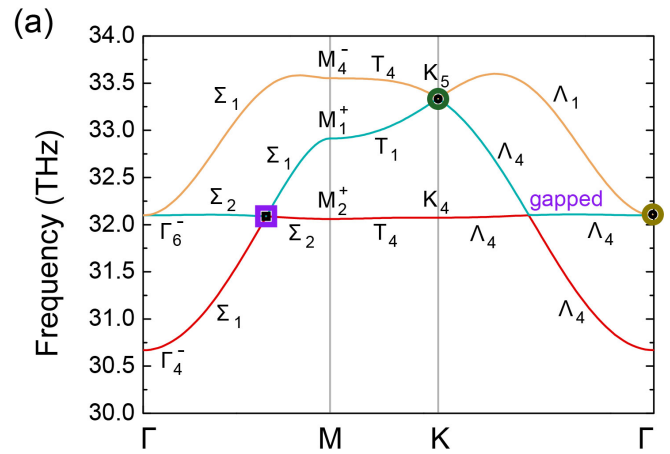

FIG. 7. (a) Phonon band-crossing points and (b) patch Euler class of undoped Al_2O_3. We use squares (circles) to represent the nodes formed by the lower (upper) two bands, open (closed) symbols to represent the nodes with negative (positive) frame charges, and one symbol (two concentric symbols) to represent the linear (quadratic) node.

stability. To be consistent with Sec. II, we use open (closed) symbols to represent the nodes with negative (positive) frame charges, as shown in Fig. 7(b).

We next compute the Euler class for all the patches containing pairs of *linear nodes*. For the neighboring dark green circles in patch 4, $\chi_{14} = 0$, indicating that these two nodes can either carry opposite frame charges or have the same frame charge with a nearby Dirac string in Δ_{13}. For convenience, we connect the neighboring pair of violet nodes in Δ_{13} in patch 5 with a violet Dirac string, and assign the same frame charge to the dark green nodes in patch 4. We also connect the pair of dark green nodes with a dark green Dirac string.

We then calculate the Euler class for all the patches containing all neighboring pairs of the violet square nodes in Δ_{13}. For patch 5, $\chi_{13} = 1$, indicating that the two nearest nodes along $\Gamma - M$ can either carry the same frame charge or have opposite frame charges with a nearby Dirac string in Δ_{14}. Because of the presence of a dark green Dirac string in their
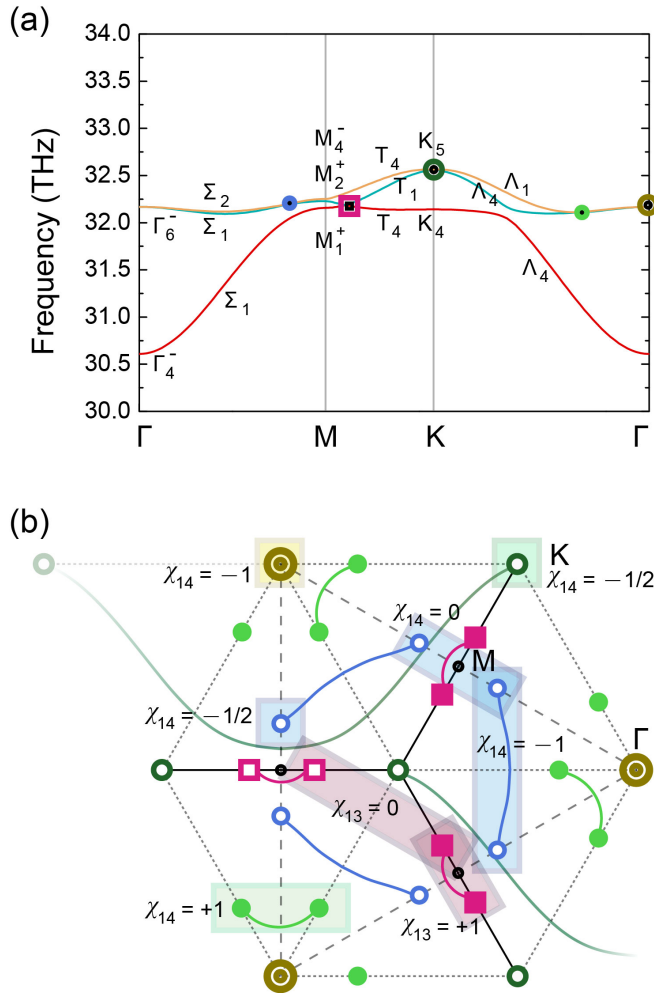
FIG. 8. (a) Phonon band-crossing points and (b) patch Euler class of -0.08 e/f.u. doped Al_2O_3.

neighboring gap Δ_{14} that crosses patch 5, we can assign the opposite frame charges to the violet nodes in Δ_{13} in patch 5. In patch 6, $\chi_{13} = 0$, and we can assign the same frame charges to the corresponding violet nodes as there is a Dirac string in Δ_{14} crossing patch 6. We then assign the Dirac strings for the neighboring violet squares, and obtain the complete global topological configuration shown in Fig. 7(b).

Finally, we check the consistency of the global topological configuration by computing the Euler class for patch 7. The calculated $\chi_{14} = -\frac{3}{2}$ is consistent with the presence of a quadratic node with $\chi_{14} = -1$ at Γ and a linear node with $\chi_{14} = -\frac{1}{2}$.

F. Frame charges of -0.08 e/f.u. doped Al_2O_3

At -0.08 e/f.u., several band inversions take place around the Γ and M high-symmetry points, as shown in Fig. 8(a). Along $\Gamma - M$ the top two bands with irreps Σ_1 and Σ_2 start to be inverted, and the top two bands along $K - \Gamma$ with irreps Λ_1 and Λ_4 are inverted as well. Because these two bands along both $\Gamma - M$ and $K - \Gamma$ have different irreps, there are two new circle nodes in Δ_{14} formed along these two high-symmetry lines, and we label the nodes along $\Gamma - M$ in blue

and those along $K - \Gamma$ in green. In addition, at the M point, bands 13 and 14 are also inverted, as the band with irrep M_1^+ now becomes lower than that with irrep M_2^+. As a result, the nodes in Δ_{13} transfer from $\Gamma - M$ to $M - K$. These band inversions significantly change the number and positions of the band nodes in gaps Δ_{13} and Δ_{14}, and the distribution of the topological frame charges is completely different from that in undoped Al_2O_3.

We start the Euler class calculations from the patches containing single nodes. The Euler class of the quadratic node at Γ and the linear node at K remains the same. All other nodes, created by the band inversions, are linear nodes as their patch Euler class is $\pm\frac{1}{2}$.

For the pink square nodes in Δ_{13} along $M - K$, the Euler class for the two pink patches, containing the first- and second-nearest neighbors in Fig. 8(b), is 1 and 0, respectively. Because there is no Dirac string in Δ_{14} crossing these two patches, we can assign the same frame charge for all the nearest pairs of pink square nodes, while keeping the second nearest pairs either with the opposite frame charges or with the same frame charge and a nearby Dirac string in Δ_{14}.

We then calculate the Euler class for pairs of the neighboring green circles in Δ_{14}, and obtain $\chi_{14} = 1$ for all the patches. Because the green circle nodes are far away from the square nodes in Δ_{13} (and their Dirac strings), we can safely assign the same frame charge for all the green circle nodes.

For the blue circle nodes along $\Gamma - M$, the patch Euler class for the nearest pair around M is 0, while the second-nearest neighbor of nodes has a patch Euler class of $\chi_{14} = -1$. Thus, we can assign all the blue circles with the same negative frame charge, with a Dirac string in Δ_{13} connecting the two pink square nodes around M. We can also connect the second-nearest neighbors of the blue circle nodes in pairs with the Dirac strings, without influencing the topological configurations in Δ_{13}.

The consistent global topological configuration is summarized in Fig. 8(b), which is also consistent with the conversion of frame charges from undoped Al_2O_3 to -0.08 e/f.u. doped Al_2O_3 (as discussed later).

G. Frame charges of -0.10 e/f.u. doped Al_2O_3

At -0.10 e/f.u., the top two bands are inverted at M, and the M_2^+ band becomes higher than the M_4^- band [Fig. 9(a)]. Consequently, the top two bands along $\Gamma - M$ are fully inverted as well, as the Σ_2 band is the highest all along the $\Gamma - M$ high-symmetry line. As a result, the blue circle nodes in Δ_{14} along $\Gamma - M$ disappear.

As the inversion of bands 14 and 15 occurs at M, the two nearest blue nodes in Δ_{14} meet each other at M. Before they meet at M, one of them must cross the pink Dirac string in Δ_{13}, which flips the sign of its frame charge. Therefore, the two blue nodes, now with the opposite frame charge, can annihilate when brought together at M. The Dirac strings of three pairs of the blue nodes now merge into a closed loop connecting the three neighboring M points, encircling the K point in the middle. By shrinking the closed Dirac string towards K, we can make it disappear, and this also flips the sign of the frame charges of the three pink nodes inside the
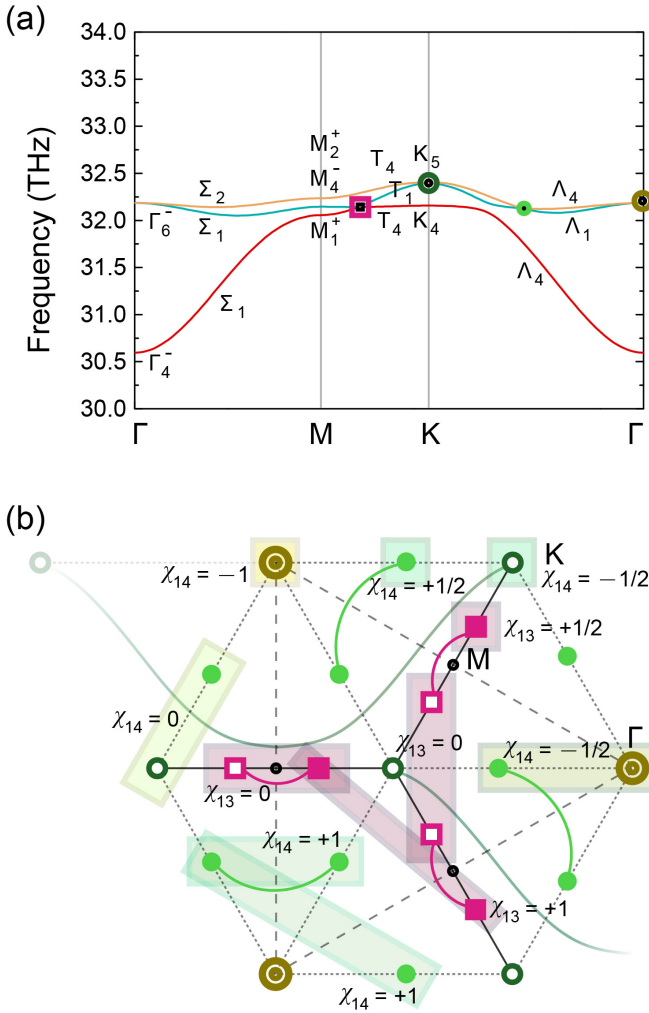
FIG. 9. (a) Phonon band-crossing points and (b) patch Euler class of -0.10 $e/$f.u. doped Al_2O_3.

FIG. 10. (a) Phonon band-crossing points and (b) patch Euler class of -0.20 $e/$f.u. doped Al_2O_3.

loop. Consequently, the two nearest pink square nodes along $M - K$ now carry opposite frame charges.

To verify this, we compute the patch Euler class in Fig. 9(b). The calculated Euler class for the pink nodes is consistent with our deduction that the two nearest pink nodes have opposite frame charges. In addition, as the braiding only takes place around M, the topological frame charges remain unchanged for other nodes away from M. This is also confirmed by our Euler class calculations.

H. Frame charges of -0.20 $e/$f.u. doped Al_2O_3

At -0.14 $e/$f.u., the doubly degenerate band with K_5 irrep becomes lower than the K_4 band, and upon further doping the topological configurations remain the same as no additional band inversion occurs. We show the phonon dispersion and the corresponding global topological configuration at -0.20 $e/$f.u. in Fig. 10 because the bands are well separated from each other at this doping density, so we can label the irreps more clearly.

We compute the Euler class for all the single nodes first, and the calculated $\chi_{14} = -1$ at Γ and $\chi_{13} = -\frac{1}{2}$ at K indicate
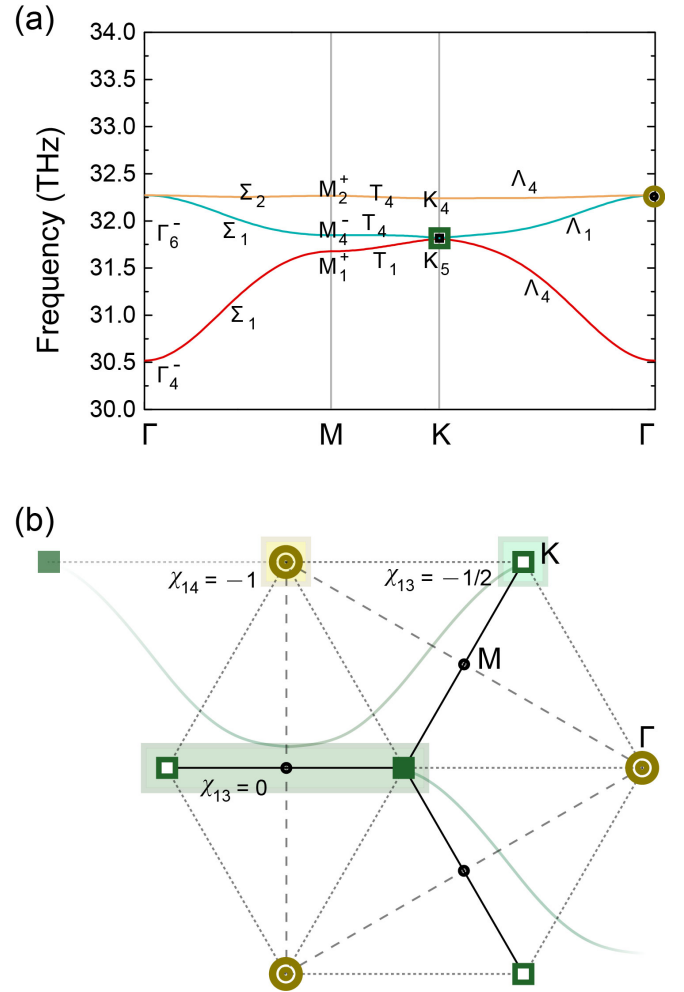
a robust quadratic node in Δ_{14} at Γ and a linear node in Δ_{13} at K. We also compute the Euler class for the patch containing two nearest K points, and obtain $\chi_{13} = 0$. Therefore, we can assign opposite frame charges to the K points, and connect each pair of them with a Dirac string.

I. Complete picture of braiding upon doping

The complete picture, summarized in Fig. 11, provides a detailed description of the conversion of non-Abelian frame charge upon electrostatic doping from -0.06 to -0.14 $e/$f.u.

From the undoped case to a doping concentration of -0.06 $e/$f.u., the band inversion between bands 13 and 14 [red and blue lines in Fig. 11(a)] becomes stronger along $\Gamma - M$, pushing the violet square nodes along $\Gamma - M$ closer to the M high-symmetry point.

Further increasing the doping concentration to -0.08 $e/$f.u. brings the two neighboring violet nodes together at M. At M, each neighboring pair of violet nodes carries the same frame charge because the nodes with opposite frame charges must cross the dark green Dirac string and the charge of one of the pairs is flipped. Therefore, the pairs of violet nodes do not annihilate. Instead, they "bounce" to the $M - K$
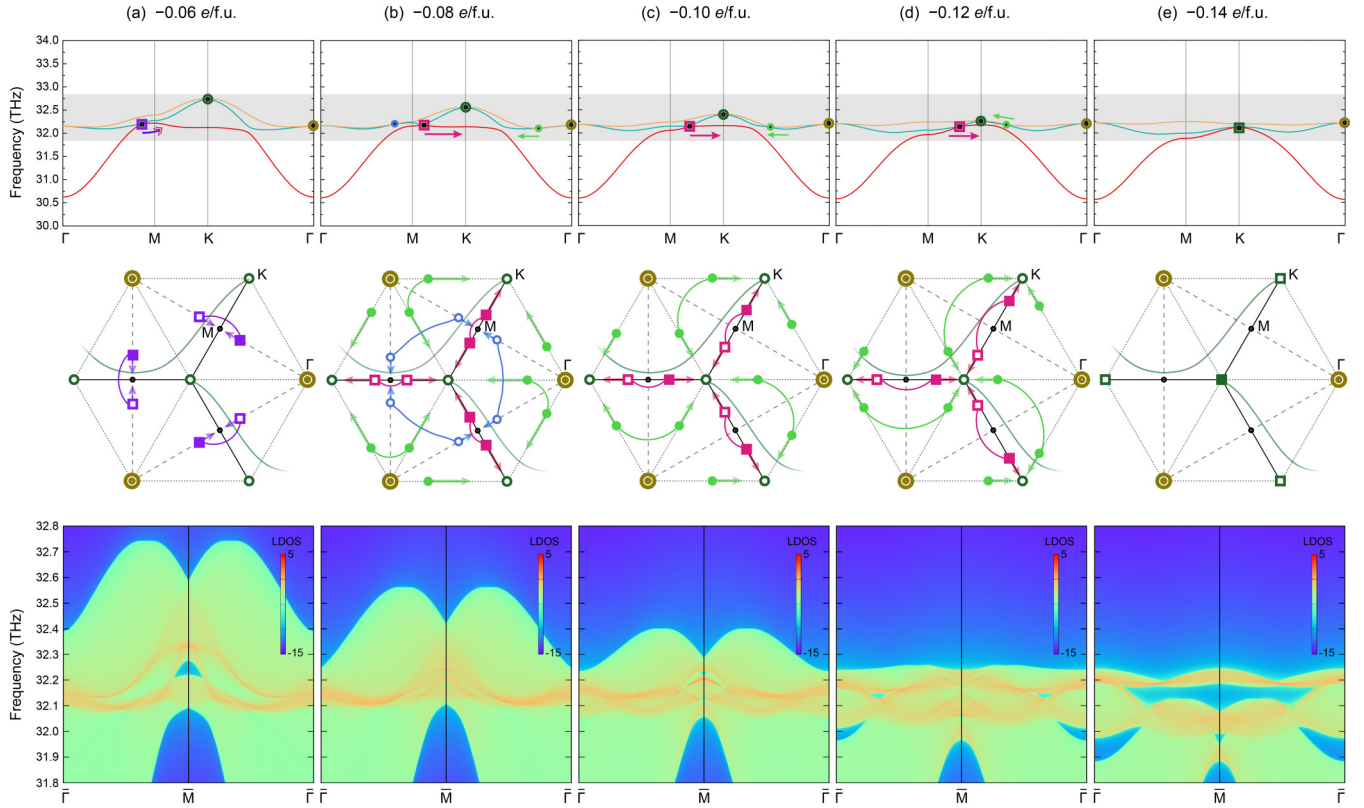
FIG. 11. Phonon spectra (top panel) and topological configurations (middle panel) of monolayer Al_2O_3 upon electrostatic doping at (a) -0.06 e/f.u., (b) -0.08 e/f.u., (c) -0.10 e/f.u., (d) -0.12 e/f.u., and (e) -0.14 e/f.u. For the topological configurations in the middle panel, we use squares (circles) to represent the nodes formed by the lower (upper) two bands, open (closed) symbols to represent the nodes with negative (positive) frame charges, and one symbol (two concentric symbols) to represent the linear (quadratic) node. The edge states along the (100) direction are also shown in the bottom panel, corresponding to the gray area of the phonon spectra in the top panel.

high-symmetry lines with each pair carrying the same frame charge, and we now label them as pink squares in Fig. 11(b) because their trajectories change. The inversion between bands 14 and 15 also creates three pairs of same charged blue nodes and three pairs of same charged green nodes along $\Gamma - M$ and $K - \Gamma$, respectively, indicating that the blue nodes must carry opposite frame charge with the green nodes so they can be created at the same time at Γ, or be annihilated simultaneously when brought back to Γ by decreasing the doping concentrations from -0.08 to -0.06 e/f.u.

At -0.10 e/f.u. the nearest pairs of the blue nodes along $\Gamma - M$ are brought together to M when the bands are fully inverted at M. During this process, one of the blue nodes in each pair must cross a Dirac string of the pink nodes and thus flips its sign. Now that each nearest pair of the blue nodes near M has the opposite frame charge, they will be annihilated when meeting at M. As shown in Fig. 11(c), at -0.10 e/f.u. the blue nodes and their corresponding Dirac strings disappear. The disappearance of the blue Dirac string also flips the sign of the three pink nodes around the K point inside the Dirac string.

At -0.12 e/f.u., the inversion between bands 13 and 14 further increases, and as a result the pink nodes move further from M to K. Similarly, the green nodes move further from Γ to K. During this process there is no conversion between the frame charges as no nodes meet together and no adjacent Dirac strings are crossed. As shown in Fig. 11(d), the global

topological configuration is nearly the same, except that the pink and green nodes move closer to K.

The braiding process ends at -0.14 e/f.u., when all the bands are fully inverted and no further inversion occurs with increasing doping concentration. When the three pink nodes and three green nodes meet at K, there are two open pink squares, one closed pink square, and three closed green circles, as well as the open dark green circle at K. We can braid the two closed green nodes with one open pink node and one closed pink node so their charges are flipped. Eventually, we will have one open pink square, two closed pink squares, one open green circle, two closed green circles, and one open dark green circle. There are two open and two closed circles in total, so the circles can be annihilated when brought together at K. The remaining open square and two closed squares can also recombine to form a closed square. Therefore, we have a closed dark green square at K in the middle of the 2D Brillouin zone in Fig. 11(e). The braiding processes around other K points are similar.

J. Topological edge states

Despite the fact that the bulk-boundary correspondence for multigap topologies has not yet been fully characterized (and is beyond the scope of this work), we can still investigate the evolution of the topological edge states of monolayer Al_2O_3 upon electrostatic doping. The surface local densities of states
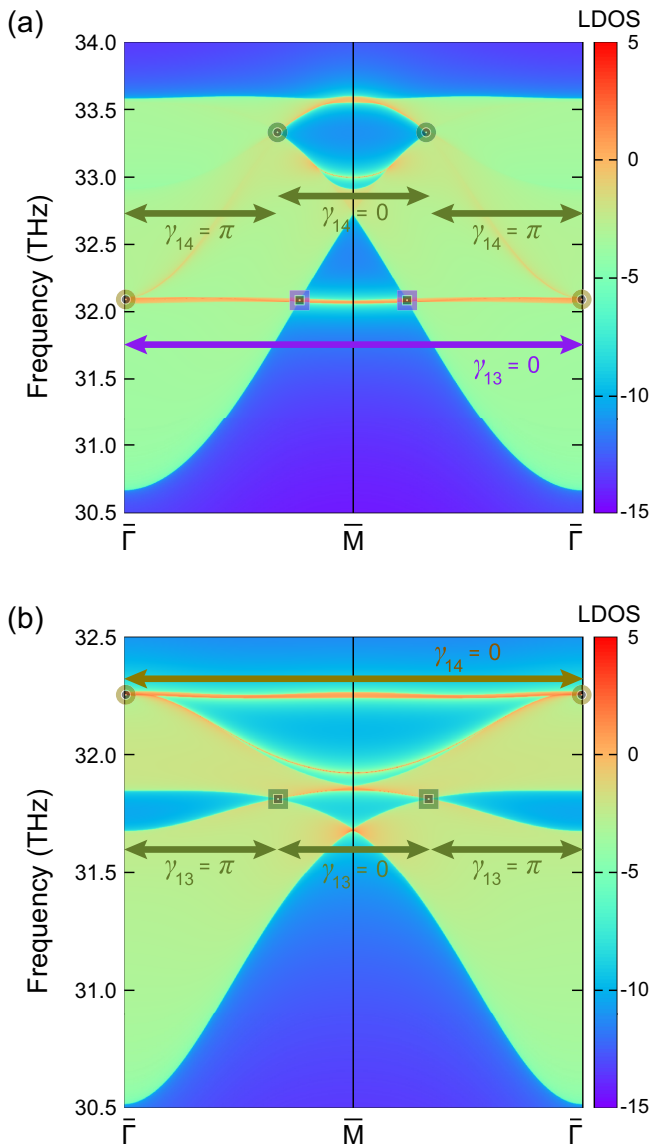
FIG. 12. Topological edge states along the (100) direction for (a) undoped and (b) $-0.20\,e/\mathrm{f.u.}$ doped Al_2O_3.

(LDOS) are calculated from the imaginary part of the surface Green's function as implemented in WANNIERTOOLS [109]. We first compare the edge states for undoped and $-0.20\,e/\mathrm{f.u.}$ doped Al_2O_3 in Fig. 12.

For undoped Al_2O_3, the edge states connecting the projections of a pair of bulk nodes in Δ_{14} at K (dark green circles) are clearly visible, as shown in Fig. 12(a). In addition, we can see the projections of the flat bulk band across the entire edge Brillouin zone, ending at the projections of a pair of bulk nodes in Δ_{14} at Γ (dark yellow circles). The emergence of the edge states can be understood by computing the Zak phase γ [111]. In Δ_{13}, we obtain $\gamma_{13} = 0$ along the entire edge Brillouin zone except at $\bar{\Gamma}$. In Δ_{14}, $\gamma_{13} = 0$ corresponds to emerging edge states between the projections of dark green nodes at K, while $\gamma_{13} = \pi$ corresponds to vanishing edge states.

For $-0.20\,e/\mathrm{f.u.}$ doped Al_2O_3, the flat band has the highest energy, and the projections of the pair of bulk nodes at Γ

(dark yellow circles) are also higher than the projections of other bulk nodes, as shown in Fig. 12(b). The edge states merge from the projections of dark yellow circles in Δ_{14} at Γ. The projections of the other pair of bulk nodes at K (dark green squares) are inverted to lower frequencies, redistributing their non-Abelian frame charges from Δ_{14} to Δ_{13}. Similar to the Zak phase in the undoped case, for $-0.20\,e/\mathrm{f.u.}$ doped Al_2O_3, $\gamma_{13} = 0$ and $\gamma_{14} = 0$ correspond to emerging edge states, while $\gamma_{13} = \pi$ corresponds to vanishing edge states.

This is consistent with the fact that the oxygen atoms, as the atomic centers, are on the boundary of the unit cell. The Zak phase measures the displacement between the Wannier functions and the atomic centers. In our case, a Zak phase of zero indicates that the phonon Wannier functions occupy the center of the unit cell and are localized away from the atomic centers on the unit-cell boundary, leading to an "anomaly" with localized edge states [55,57]. On the other hand, a Zak phase of π indicates that the phonon Wannier states and the atoms are at the same places on the unit-cell boundary, corresponding to vanishing edge states. While this $\mathbb{Z}_2$-quantized Berry phase is a good quantum number for 1D edge states [111] and traces in *some* gaps the edge states faithfully, we repeat that a full bulk boundary relation describing topological phases obtained by non-Abelian processes is still subject to intense research activity.

We also show the evolution of the edge states under phonon braiding upon electrostatic doping from -0.06 to $-0.14\,e/\mathrm{f.u.}$ in the bottom panel of Fig. 11, which can provide information on the conversion of non-Abelian frame charges in the bulk states. Because the bulk nodes are distributed in a narrow frequency range between 31.8–32.8 THz, the topological edge states are not well separated from each other.

V. DISCUSSION

Our findings of Sec. IV suggest a broad relevance to the fields of topology, phonons, dielectrics, first principles-modeling, and information storage.

From a topological perspective, we find that phonons can be a primary platform to study multigap topologies. When studying multigap topologies in electronic systems, all three neighboring bands must be near the Fermi level, which severely limits the potential material candidates. On the other hand, phonons do not have the restriction of the Fermi level because they are bosonic excitations. In addition, the time-reversal symmetry T in phononic systems is hard to break, making it more convenient to find material candidates with C_2T symmetry or PT symmetry. As phonons can be treated as spinless systems, we can apply several existing models, such as the three-band spinless model with a kagome lattice [55], to phononic systems. We can also extend the ideas of non-Abelian braiding to other quasiparticles such as magnons [112] and excitons [113]. An open question is the bulk-boundary correspondence of multigap topologies, and phonon dispersions with fewer, cleaner band crossings, e.g., phonon systems with only one or two atoms in the unit cell, could provide an ideal platform for its study.

For the phonon community, we open a research direction for these emergent excitations. Traditional studies of phonons mainly involve conventional superconductivity [114,115],

electrical and thermal transport [116–120], carrier thermalization [121,122], structural phase transition [123,124], and charge density waves [125,126]. Here, we show that the reciprocal space braiding of phonon band-crossing points can also form the basis for next-generation phononic computation. Several strategies could be used to experimentally verify the non-Abelian braiding of phonons, including inelastic neutron scattering [69,127,128], inelastic x-ray scattering [66], and high-resolution electron energy-loss spectroscopy [129]. Additionally, our first-principles evaluation of the band inversion processes can provide references for the experimental observation of the evolution of the phonon band nodes upon electrostatic doping. Another open question is whether the band inversion at K can be measured by double-resonance Raman modes [130] when the energy and momentum conservations are fulfilled [106].

For dielectrics, we provide an experimentally realizable way to control the braiding in a well-known dielectric material upon electrostatic doping. Monolayer Al_2O_3 has been widely used as a gate dielectric in electronic devices [84–87]. Therefore, electrostatic doping of monolayer Al_2O_3 can be experimentally feasible and has the potential to be incorporated into existing devices based on Al_2O_3, opening the door for studying topology-related phenomena in this otherwise well-studied material. In addition, electrostatic doping-induced phonon shifts have been intensively studied in low-dimensional materials, which can be probed directly using Raman spectroscopy [107,131]. We would also like to highlight that applying an electric field of 0.65–0.95 eV/Å has similar effects on phonon band inversion and the corresponding braiding processes [106]. It is therefore interesting to investigate how doping or gating redistributes the charge density and how the redistributed charge couples to the lattice vibrational modes.

For first-principles modeling, we note that the computational techniques described in this paper offer a route to understand non-Abelian braiding of *any quasiparticle*. The Euler class can be computed using the eigenvectors and eigenstates of these quasiparticles as input. We offer a detailed description of all the theoretical background and computational methodology to analyze the non-Abelian frame charges formed by any three-band subsystems in the spectra of any quasiparticle, as long as the symmetry requirements are fulfilled. We anticipate that the potential braiding processes rely on control of band inversion and the corresponding redistribution of non-Abelian frame charge. Future simulation work could focus on various strategies to control the phonon braiding, including nonlinear effects [132–135], anharmonicity [127,136–139], and ultrafast pumps [140–143].

Finally, as a further distant and more speculative perspective, the braid processes might find use in storing information. The idea is that information may be robust against perturbations from the environment because the nontrivial frame charges can only become trivial by unbraiding the non-Abelian frame charges via introducing a third phonon band. In addition, we can control these non-Abelian frame charges and their braiding by electrostatic doping, offering new opportunities for a conceptually new computation hardware based on phonons. Moreover, the braiding of multiple nodes takes place simultaneously when these nodes are related to each other by the space-group symmetry, suggesting the possibility of storing information in the frame charges combining the topological and the symmetry information together. While we foresee that such information could be encoded in phonons, this nevertheless leaves open the exciting question of whether phonons could be suitable to implement quantum algorithms.

[1] A. Stern, Nature (London) **464**, 187 (2010).

[2] S. Das Sarma, M. Freedman, and C. Nayak, Phys. Rev. Lett. **94**, 166802 (2005).

[3] S. Das Sarma, C. Nayak, and S. Tewari, Phys. Rev. B **73**, 220502(R) (2006).

[4] L. Fu and C. L. Kane, Phys. Rev. Lett. **100**, 096407 (2008).

[5] T. Iadecola, T. Schuster, and C. Chamon, Phys. Rev. Lett. **117**, 073901 (2016).

[6] M. Ezawa, Phys. Rev. B **102**, 075424 (2020).

[7] S. Nadj-Perge, I. K. Drozdov, J. Li, H. Chen, S. Jeon, J. Seo, A. H. MacDonald, B. A. Bernevig, and A. Yazdani, Science **346**, 602 (2014).

[8] D. Wang, L. Kong, P. Fan, H. Chen, S. Zhu, W. Liu, L. Cao, Y. Sun, S. Du, J. Schneeloch, R. Zhong, G. Gu, L. Fu, H. Ding, and H.-J. Gao, Science **362**, 333 (2018).

[9] H. Zhang, C.-X. Liu, S. Gazibegovic, D. Xu, J. A. Logan, G. Wang, N. van Loo, J. D. S. Bommer, M. W. A. de Moor, D. Car, R. L. M. Op het Veld, P. J. van Veldhoven, S. Koelling, M. A. Verheijen, M. Pendharkar, D. J. Pennachio, B. Shojaei, J. S. Lee, C. J. Palmstrøm, E. P. A. M. Bakkers *et al.*, Nature (London) **556**, 74 (2018).

[10] R.-J. Slager, A. Mesaros, V. Juričić, and J. Zaanen, Nat. Phys. **9**, 98 (2013).

[11] B. A. Bernevig, T. L. Hughes, and Z. Shou-Cheng, Science **314**, 1757 (2006).

[12] L. Fu, Phys. Rev. Lett. **106**, 106802 (2011).

[13] V. Juričić, A. Mesaros, R.-J. Slager, and J. Zaanen, Phys. Rev. Lett. **108**, 106403 (2012).

[14] T. L. Hughes, E. Prodan, and B. A. Bernevig, Phys. Rev. B **83**, 245132 (2011).

[15] A. M. Turner, Y. Zhang, R. S. K. Mong, and A. Vishwanath, Phys. Rev. B **85**, 165120 (2012).

[16] C. Fang, M. J. Gilbert, and B. A. Bernevig, Phys. Rev. B **86**, 115112 (2012).

[17] D. Rainis, L. Trifunovic, J. Klinovaja, and D. Loss, Phys. Rev. B **87**, 024515 (2013).

[18] R.-J. Slager, A. Mesaros, V. Juričić, and J. Zaanen, Phys. Rev. B **90**, 241403(R) (2014).

[19] K. Shiozaki and M. Sato, Phys. Rev. B **90**, 165114 (2014).

[20] A. Alexandradinata, X. Dai, and B. A. Bernevig, Phys. Rev. B **89**, 155114 (2014).

[21] R.-J. Slager, L. Rademaker, J. Zaanen, and L. Balents, Phys. Rev. B **92**, 085126 (2015).

[22] C.-K. Chiu, J. C. Y. Teo, A. P. Schnyder, and S. Ryu, Rev. Mod. Phys. **88**, 035005 (2016).

[23] K. Shiozaki, M. Sato, and K. Gomi, Phys. Rev. B **95**, 235425 (2017).

[24] A. Bouhon and A. M. Black-Schaffer, Phys. Rev. B **95**, 241101(R) (2017).

[25] J. Kruthoff, J. de Boer, J. van Wezel, C. L. Kane, and R.-J. Slager, Phys. Rev. X **7**, 041069 (2017).

[26] H. C. Po, A. Vishwanath, and H. Watanabe, Nat. Commun. **8**, 50 (2017).

[27] B. Bradlyn, L. Elcoro, J. Cano, M. G. Vergniory, Z. Wang, C. Felser, M. I. Aroyo, and B. A. Bernevig, Nature (London) **547**, 298 (2017).

[28] J.-W. Rhim, J. H. Bardarson, and R.-J. Slager, Phys. Rev. B **97**, 115143 (2018).

[29] R.-J. Slager, J. Phys. Chem. Solids **128**, 24 (2019).

[30] M. Nakagawa, R.-J. Slager, S. Higashikawa, and T. Oka, Phys. Rev. B **101**, 075108 (2020).

[31] F. N. Ünal, A. Eckardt, and R.-J. Slager, Phys. Rev. Research **1**, 022003(R) (2019).

[32] M. S. Scheurer and R.-J. Slager, Phys. Rev. Lett. **124**, 226401 (2020).

[33] A. Alexandradinata, J. Höller, C. Wang, H. Cheng, and L. Lu, Phys. Rev. B **102**, 115117 (2020).

[34] E. Cornfeld and S. Carmeli, Phys. Rev. Research **3**, 013052 (2021).

[35] T. T. Heikkilä, N. B. Kopnin, and G. E. Volovik, JETP Lett. **94**, 233 (2011).

[36] S.-Y. Xu, I. Belopolski, N. Alidoust, M. Neupane, G. Bian, C. Zhang, R. Sankar, G. Chang, Z. Yuan, C.-C. Lee, S.-M. Huang, H. Zheng, J. Ma, D. S. Sanchez, B. Wang, A. Bansil, F. Chou, P. P. Shibayev, H. Lin, S. Jia, and M. Z. Hasan, Science **349**, 613 (2015).

[37] B. Q. Lv, H. M. Weng, B. B. Fu, X. P. Wang, H. Miao, J. Ma, P. Richard, X. C. Huang, L. X. Zhao, G. F. Chen, Z. Fang, X. Dai, T. Qian, and H. Ding, Phys. Rev. X **5**, 031013 (2015).

[38] L. X. Yang, Z. K. Liu, Y. Sun, H. Peng, H. F. Yang, T. Zhang, B. Zhou, Y. Zhang, Y. F. Guo, M. Rahn, D. Prabhakaran, Z. Hussain, S.-K. Mo, C. Felser, B. Yan, and Y. L. Chen, Nat. Phys. **11**, 728 (2015).

[39] C. Fang, Y. Chen, H.-Y. Kee, and L. Fu, Phys. Rev. B **92**, 081201(R) (2015).

[40] H. Huang, J. Liu, D. Vanderbilt, and W. Duan, Phys. Rev. B **93**, 201114(R) (2016).

[41] J. Hu, Z. Tang, J. Liu, X. Liu, Y. Zhu, D. Graf, K. Myhro, S. Tran, C. N. Lau, J. Wei, and Z. Mao, Phys. Rev. Lett. **117**, 016602 (2016).

[42] S.-Y. Yang, H. Yang, E. Derunova, S. S. P. Parkin, B. Yan, and M. N. Ali, Adv. Phys.: X **3**, 1414631 (2018).

[43] N. P. Armitage, E. J. Mele, and A. Vishwanath, Rev. Mod. Phys. **90**, 015001 (2018).

[44] B. Peng, C. Yue, H. Zhang, Z. Fang, and H. Weng, npj Comput. Mater. **4**, 68 (2018).

[45] B. Peng, I. Bravić, J. L. MacManus-Driscoll, and B. Monserrat, Phys. Rev. B **100**, 161101(R) (2019).

[46] S. A. Díaz, J. Klinovaja, and D. Loss, Phys. Rev. Lett. **122**, 187203 (2019).

[47] A. Bouhon, T. Bzdušek, and R.-J. Slager, Phys. Rev. B **102**, 115135 (2020).

[48] J. Ahn, S. Park, and B.-J. Yang, Phys. Rev. X **9**, 021013 (2019).

[49] J. Ahn and B.-J. Yang, Phys. Rev. B **99**, 235125 (2019).

[50] A. Bouhon, Q. Wu, R.-J. Slager, H. Weng, O. V. Yazyev, and T. Bzdušek, Nat. Phys. **16**, 1137 (2020).

[51] A. Tiwari and T. Bzdušek, Phys. Rev. B **101**, 195130 (2020).

[52] F. N. Ünal, A. Bouhon, and R.-J. Slager, Phys. Rev. Lett. **125**, 053601 (2020).

[53] A. Bouhon, A. M. Black-Schaffer, and R.-J. Slager, Phys. Rev. B **100**, 195135 (2019).

[54] Q. Wu, A. A. Soluyanov, and T. Bzdušek, Science **365**, 1273 (2019).

[55] B. Jiang, A. Bouhon, Z.-K. Lin, X. Zhou, B. Hou, F. Li, R.-J. Slager, and J.-H. Jiang, Nat. Phys. **17**, 1239 (2021).

[56] A. Bouhon, G. F. Lange, and R.-J. Slager, Phys. Rev. B **103**, 245127 (2021).

[57] G. F. Lange, A. Bouhon, and R.-J. Slager, arXiv:2109.01676.

[58] B. Peng, A. Bouhon, B. Monserrat, and R.-J. Slager, Nat. Commun. **13**, 423 (2022).

[59] S. Chen, A. Bouhon, R.-J. Slager, and B. Monserrat, arXiv:2108.10330.

[60] V. Könye, A. Bouhon, I. C. Fulga, R.-J. Slager, J. van den Brink, and J. I. Facio, Phys. Rev. Research **3**, L042017 (2021).

[61] Y. X. Zhao and Y. Lu, Phys. Rev. Lett. **118**, 056401 (2017).

[62] B. J. Wieder and B. A. Bernevig, arXiv:1810.02373.

[63] A. J. Beekman, J. Nissinen, K. Wu, K. Liu, R.-J. Slager, Z. Nussinov, V. Cvetkovic, and J. Zaanen, Phys. Rep. **683**, 1 (2017).

[64] O. Stenull, C. L. Kane, and T. C. Lubensky, Phys. Rev. Lett. **117**, 068001 (2016).

[65] T. Zhang, Z. Song, A. Alexandradinata, H. Weng, C. Fang, L. Lu, and Z. Fang, Phys. Rev. Lett. **120**, 016401 (2018).

[66] H. Miao, T. T. Zhang, L. Wang, D. Meyers, A. H. Said, Y. L. Wang, Y. G. Shi, H. M. Weng, Z. Fang, and M. P. M. Dean, Phys. Rev. Lett. **121**, 035302 (2018).

[67] J. Li, Q. Xie, S. Ullah, R. Li, H. Ma, D. Li, Y. Li, and X.-Q. Chen, Phys. Rev. B **97**, 054305 (2018).

[68] B. W. Xia, R. Wang, Z. J. Chen, Y. J. Zhao, and H. Xu, Phys. Rev. Lett. **123**, 065501 (2019).

[69] T. T. Zhang, H. Miao, Q. Wang, J. Q. Lin, Y. Cao, G. Fabbris, A. H. Said, X. Liu, H. C. Lei, Z. Fang, H. M. Weng, and M. P. M. Dean, Phys. Rev. Lett. **123**, 245302 (2019).

[70] Y. Liu, X. Chen, and Y. Xu, Adv. Funct. Mater. **30**, 1904784 (2020).

[71] J. Li, J. Liu, S. A. Baronett, M. Liu, L. Wang, R. Li, Y. Chen, D. Li, Q. Zhu, and X.-Q. Chen, Nat. Commun. **12**, 1204 (2021).

[72] B. Peng, Y. Hu, S. Murakami, T. Zhang, and B. Monserrat, Sci. Adv. **6**, eabd1618 (2020).

[73] Q.-B. Liu, Y. Qian, H.-H. Fu, and Z. Wang, npj Comput. Mater. **6**, 95 (2020).

[74] Z. Wang, W. Zhou, A. N. Rudenko, and S. Yuan, Phys. Rev. B **103**, 195137 (2021).

[75] D.-S. Tang and B.-Y. Cao, J. Appl. Phys. **129**, 085102 (2021).

[76] Q.-B. Liu, H.-H. Fu, and R. Wu, Phys. Rev. B **104**, 045409 (2021).

[77] P.-F. Liu, J. Li, X.-H. Tu, H. Li, J. Zhang, P. Zhang, Q. Gao, and B.-T. Wang, Phys. Rev. B **103**, 094306 (2021).

[78] Q.-B. Liu, Z.-Q. Wang, and H.-H. Fu, Phys. Rev. B **104**, L041405 (2021).

[79] J.-Y. You, X.-L. Sheng, and G. Su, Phys. Rev. B **103**, 165143 (2021).

[80] C. Xie, Y. Liu, Z. Zhang, F. Zhou, T. Yang, M. Kuang, X. Wang, and G. Zhang, Phys. Rev. B **104**, 045148 (2021).

[81] B. Zheng, F. Zhan, X. Wu, R. Wang, and J. Fan, Phys. Rev. B **104**, L060301 (2021).

[82] J. Wang, H. Yuan, M. Kuang, T. Yang, Z.-M. Yu, Z. Zhang, and X. Wang, Phys. Rev. B **104**, L041107 (2021).

[83] B. Peng, S. Murakami, B. Monserrat, and T. Zhang, npj Comput. Mater. **7**, 195 (2021).

[84] D. C. Gilmer, R. Hegde, R. Cotton, R. Garcia, V. Dhandapani, D. Triyoso, D. Roan, A. Franke, R. Rai, L. Prabhu, C. Hobbs, J. M. Grant, L. La, S. Samavedam, B. Taylor, H. Tseng, and P. Tobin, Appl. Phys. Lett. **81**, 1288 (2002).

[85] K. Hirama, H. Sato, Y. Harada, H. Yamamoto, and M. Kasu, Jpn. J. Appl. Phys. **51**, 090114 (2012).

[86] Z. Ren, J. Zhang, J. Zhang, C. Zhang, S. Xu, Y. Li, and Y. Hao, IEEE Electron Device Lett. **38**, 786 (2017).

[87] H.-M. Kwon, D.-H. Kim, and T.-W. Kim, Electronics **9**, 2039 (2020).

[88] N. Johansson and E. Sjöqvist, Phys. Rev. Lett. **92**, 060406 (2004).

[89] J. Ahn, D. Kim, Y. Kim, and B.-J. Yang, Phys. Rev. Lett. **121**, 106403 (2018).

[90] F. Xie, Z. Song, B. Lian, and B. A. Bernevig, Phys. Rev. Lett. **124**, 167002 (2020).

[91] M. Born and K. Huang, Dynamical Theory of Crystal Lattices (Clarendon, Oxford, 1954).

[92] A. Togo and I. Tanaka, Scr. Mater. **108**, 1 (2015).

[93] A. Togo, F. Oba, and I. Tanaka, Phys. Rev. B **78**, 134106 (2008).

[94] K. Kunc and R. M. Martin, Phys. Rev. Lett. **48**, 406 (1982).

[95] D. Alfè, Comput. Phys. Commun. **180**, 2622 (2009).

[96] B. Monserrat, J. Phys.: Condens. Matter **30**, 083001 (2018).

[97] S. Baroni, S. de Gironcoli, A. Dal Corso, and P. Giannozzi, Rev. Mod. Phys. **73**, 515 (2001).

[98] M. T. Dove, Introduction to Lattice Dynamics (Cambridge University Press, Cambridge, 1993).

[99] J. M. Ziman, in Electrons and Phonons: The Theory of Transport Phenomena in Solids, edited by E. C. B. N. F. Mott and D. H. Wilkinson (Oxford University Press, Oxford, 1960).

[100] G. P. Srivastava, The Physics of Phonons (Hilger, Bristol, 1990).

[101] A. M. Chebotarev and A. E. Teretenkov, Appl. Math. Computat. **234**, 380 (2014).

[102] T. Bzdušek, ResearchGate (2019).

[103] G. Kresse and J. Furthmüller, Phys. Rev. B **54**, 11169 (1996).

[104] G. Kresse and J. Furthmüller, Comput. Mater. Sci. **6**, 15 (1996).

[105] J. P. Perdew, A. Ruzsinszky, G. I. Csonka, O. A. Vydrov, G. E. Scuseria, L. A. Constantin, X. Zhou, and K. Burke, Phys. Rev. Lett. **100**, 136406 (2008).

[106] See Supplemental Material at http://link.aps.org/supplemental/10.1103/PhysRevB.105.085115 for the extra charge distribution upon hole doping; for the convergence test with respect to the supercell size; for the convergence test with respect to the vacuum spacing; for the phonon spectra upon electron doping; for the full phonon dispersion upon hole doping; for the possible scattering process; for the phonon band inversion under an electric field.

[107] T. Sohier, E. Ponomarev, M. Gibertini, H. Berger, N. Marzari, N. Ubrig, and A. F. Morpurgo, Phys. Rev. X **9**, 031019 (2019).

[108] T. Sohier, M. Gibertini, M. Calandra, F. Mauri, and N. Marzari, Nano Lett. **17**, 3758 (2017).

[109] Q. Wu, S. Zhang, H.-F. Song, M. Troyer, and A. A. Soluyanov, Comput. Phys. Commun. **224**, 405 (2018).

[110] T. T. Song, M. Yang, J. W. Chai, M. Callsen, J. Zhou, T. Yang, Z. Zhang, J. S. Pan, D. Z. Chi, Y. P. Feng, and S. J. Wang, Sci. Rep. **6**, 29221 (2016).

[111] J. Zak, Phys. Rev. Lett. **62**, 2747 (1989).

[112] F.-Y. Li, Y.-D. Li, Y. B. Kim, L. Balents, Y. Yu, and G. Chen, Nat. Commun. **7**, 12691 (2016).

[113] F. Wu, T. Lovorn, and A. H. MacDonald, Phys. Rev. Lett. **118**, 147401 (2017).

[114] A. P. Drozdov, M. I. Eremets, I. A. Troyan, V. Ksenofontov, and S. I. Shylin, Nature (London) **525**, 73 (2015).

[115] K. Ahadi, L. Galletti, Y. Li, S. Salmani-Rezaie, W. Wu, and S. Stemmer, Sci. Adv. **5**, eaaw0120 (2019).

[116] B. Peng, H. Zhang, H. Shao, H. Lu, D. W. Zhang, and H. Zhu, Nano Energy **30**, 225 (2016).

[117] B. Peng, Z. Ning, H. Zhang, H. Shao, Y. Xu, G. Ni, and H. Zhu, J. Phys. Chem. C **120**, 29324 (2016).

[118] B. Peng, H. Zhang, H. Shao, K. Xu, G. Ni, J. Li, H. Zhu, and C. M. Soukoulis, J. Mater. Chem. A **6**, 2018 (2018).

[119] B. Peng, B. Mortazavi, H. Zhang, H. Shao, K. Xu, J. Li, G. Ni, T. Rabczuk, and H. Zhu, Phys. Rev. Appl. **10**, 034046 (2018).

[120] B. Peng, H. Mei, H. Zhang, H. Shao, K. Xu, G. Ni, Q. Jin, C. M. Soukoulis, and H. Zhu, Inorg. Chem. Front. **6**, 920 (2019).

[121] M. Bernardi, D. Vigil-Fowler, J. Lischner, J. B. Neaton, and S. G. Louie, Phys. Rev. Lett. **112**, 257402 (2014).

[122] Z. Li, B. Peng, M.-L. Lin, Y.-C. Leng, B. Zhang, C. Pang, P.-H. Tan, B. Monserrat, and F. Chen, npj 2D Mater. Appl. **5**, 87 (2021).

[123] B. Peng, H. Zhang, W. Chen, B. Hou, Z.-J. Qiu, H. Shao, H. Zhu, B. Monserrat, D. Fu, H. Weng, and C. M. Soukoulis, npj 2D Mater. Appl. **4**, 14 (2020).

[124] F. Gu, E. Murray, and P. Tangney, Phys. Rev. Materials **5**, 034414 (2021).

[125] H. M. Hill, S. Chowdhury, J. R. Simpson, A. F. Rigosi, D. B. Newell, H. Berger, F. Tavazza, and A. R. Hight Walker, Phys. Rev. B **99**, 174110 (2019).

[126] L. Yue, S. Xue, J. Li, W. Hu, A. Barbour, F. Zheng, L. Wang, J. Feng, S. B. Wilkins, C. Mazzoli, R. Comin, and Y. Li, Nat. Commun. **11**, 98 (2020).

[127] X. He, D. Bansal, B. Winn, S. Chi, L. Boatner, and O. Delaire, Phys. Rev. Lett. **124**, 145901 (2020).

[128] N. Choudhury, E. J. Walter, A. I. Kolesnikov, and C.-K. Loong, Phys. Rev. B **77**, 134111 (2008).

[129] X. Jia, S. Zhang, R. Sankar, F.-C. Chou, W. Wang, K. Kempa, E. W. Plummer, J. Zhang, X. Zhu, and J. Guo, Phys. Rev. Lett. **119**, 136805 (2017).

[130] H. Guo, T. Yang, M. Yamamoto, L. Zhou, R. Ishikawa, K. Ueno, K. Tsukagoshi, Z. Zhang, M. S. Dresselhaus, and R. Saito, Phys. Rev. B **91**, 205415 (2015).

[131] L. Zhang, L. Huang, S. P. O'Brien, and Z. Yu, J. Phys. Chem. C **112**, 20118 (2008).

[132] D. M. Juraschek, M. Fechner, and N. A. Spaldin, Phys. Rev. Lett. **118**, 054101 (2017).

[133] G. Khalsa and N. A. Benedek, npj Quant. Mater. **3**, 15 (2018).

[134] D. M. Juraschek, T. c. v. Neuman, J. Flick, and P. Narang, Phys. Rev. Research **3**, L032046 (2021).

[135] G. Khalsa, N. A. Benedek, and J. Moses, Phys. Rev. X **11**, 021067 (2021).

[136] M. Borinaga, I. Errea, M. Calandra, F. Mauri, and A. Bergara, Phys. Rev. B **93**, 174308 (2016).

[137] M. Boukhicha, M. Calandra, M.-A. Measson, O. Lancry, and A. Shukla, Phys. Rev. B **87**, 195316 (2013).

[138] K. H. Michel, S. Costamagna, and F. M. Peeters, Phys. Rev. B **91**, 134302 (2015).

[139] L. D. Whalley, J. M. Skelton, J. M. Frost, and A. Walsh, Phys. Rev. B **94**, 220301(R) (2016).

[140] K. Ishioka, M. Hase, M. Kitajima, L. Wirtz, A. Rubio, and H. Petek, Phys. Rev. B **77**, 121402(R) (2008).

[141] S. Reichardt and L. Wirtz, Sci. Adv. **6**, eabb5915 (2020).

[142] C. Trovatello, H. P. C. Miranda, A. Molina-Sánchez, R. Borrego-Varillas, C. Manzoni, L. Moretti, L. Ganzer, M. Maiuri, J. Wang, D. Dumcenco, A. Kis, L. Wirtz, A. Marini, G. Soavi, A. C. Ferrari, G. Cerullo, D. Sangalli, and S. D. Conte, ACS Nano **14**, 5700 (2020).

[143] D. Karlsson, R. van Leeuwen, Y. Pavlyukh, E. Perfetto, and G. Stefanucci, Phys. Rev. Lett. **127**, 036402 (2021).

[144] www.hpc.cam.ac.uk.